UNIVERSITY OF OKLAHOMA

GRADUATE COLLEGE

AN APPARATUS TO STUDY MATTER-WAVE QUANTUM OPTICS IN SODIUM SPINOR BOSE-EINSTEIN CONDENSATES

A THESIS

SUBMITTED TO THE GRADUATE FACULTY

in partial fulfillment of the requirements for the

Degree of

MASTER OF SCIENCE

By

ANITA BHAGAT
Norman, Oklahoma
2017

AN APPARATUS TO STUDY MATTER-WAVE QUANTUM OPTICS IN SODIUM SPINOR BOSE-EINSTEIN CONDENSATES

A THESIS APPROVED FOR THE
HOMER L. DODGE DEPARTMENT OF PHYSICS AND ASTRONOMY

BY

Dr. Arne Schwettmann, Chair

Dr. James P. Shaffer

Dr. Alberto Marino

Dedicated

To

My parents

For supporting and encouraging me to believe in myself.

My lovely brothers Arun and Aditya and my cutest sister Ankita

For their love, care and laughter which kept me smiling and inspired.

Finally,*my friend Avinash*

For always being there as my unconditional friend and encouraging me to pursue the path of my passion.

Acknowledgements

First, I would like to thank my thesis advisor Dr. Arne Schwettmann at The University of Oklahoma for constant enthusiasm. He always showed patience and have time in explaining me complicated physics theories and models. He always lead me in the right direction whenever I was in need of one.

I would also like to thank my undergraduate research advisors, Dr. Carl H. Sondergeld from the petroleum engineering department and Dr. Kieran Mullen from the physics department at The University of Oklahoma. I thank Dr. Sondergeld for being the first person to teach me how to do research and analyze data, and Dr. Mullen for encouraging and guiding me over the years.

Finally, I would also like to thank my labmates Qimin Zhang and Shan Zhong for the refreshing discussions and working together long hours in lab to get things done.

Table of Contents

List of Tables

List of Figures

Abstract

Spin-exchange collisions in quantum degenerate gases act as a nonlinear interaction that creates entanglement between atoms in different spin states. Therefore, they make it possible to study matter-wave quantum nonlinear optics in spin space. In my work towards creating a spinor Bose-Einstein condensate of sodium to study these collisions, I made improvements to a laser cooling and trapping apparatus that are detailed in this thesis. I implemented and tested an imaging system for absorption and fluorescence imaging. I used this imaging system to optimize a laser cooling and trapping apparatus to yield trapped atom numbers of $6.0(3) \times 10^8$ and sub-Doppler temperatures of $65.0(1)$ μK. These numbers and temperatures provide a good starting point for further cooling via forced evaporation in a crossed optical dipole trap and will allow the group to reach Bose-Einstein condensate temperatures of ~ 100 nK in the near future.

Chapter 1

Introduction

This chapter includes a general overview and an outline of the thesis content.

1.1 Overview

Since the first experimental observations in 1995 [4, 5], Bose-Einstein condensates (BECs) of ultracold atomic gases have been the subject of intense research. BECs provide the possibility to study quantum phenomena at macroscopic scales. Initially, research of this new form of matter that exists at ultracold temperatures ~ 100 nK focused on the dynamics and excitations of BEC in magnetic traps. Typically, in magnetic traps, all but one spin state are ejected from the trap and spin dynamics cannot be studied. With the advent of all-optical trapping methods, multiple spin states could be trapped simultaneously to form a spinor BEC [6]. A spinor BEC is described by a multi-component order parameter. In a spinor BEC, the liberated spin degree of freedom allows for coherent spin dynamics driven by spin-changing collisions. These dynamics open the door for studies of matter-wave quantum optics in spin space, where different spin states of atoms in the BEC play the role of probe, conjugate, and pump beams of light as in nonlinear optics. Our group at the University of Oklahoma has been working towards the experimental realization of a F =1 ^{23}Na spinor BEC to study matter-wave interferometry in spin space. This kind of quantum interferometry in spin space is possible because of the precise control of coherent collisional spin dynamics in the spinor BEC system via microwave-dressing.

The main objective of this thesis is to present the recent experimental work done in our group towards achieving BEC. The most efficient method to obtain a BEC is to first implement a magneto-optical trap (MOT). This method uses both a laser system

and an inhomogenous magnetic field to cool and trap a gas of atoms in an ultra high vacuum system. I focus on my part of the work which consisted of characterizing the MOT and optimizing the density and the temperature of the MOT. The optimization is done via an absorption imaging system that I implemented, and via controlled timing of a cooling sequence where we switch magnetic fields, laser powers, laser detunings, and other parameters with a computer system. The MOT is the first step in the realization of a BEC. The optimization of the atomic number in the MOT is very important as there is a large loss of atoms when transferring the cloud from the MOT into an all-optical trap in order to lower the temperature to the nanokelvin regime. To perform future experiments it is good to have the largest possible number of atoms in the MOT as it will increase the probability of having higher number of atoms in the BEC and therefore allow for a better signal-to-noise ratio in experiments. In the MOT, the atoms are trapped and pre-cooled to temperatures around the Doppler limit which is T = 240 μK for ^{23}Na. Atoms are then further cooled to several microkelvin using polarization gradient cooling in an optical molasses stage that I implemented as discussed in this thesis.

1.2 Outline of the thesis

The thesis is organized and divided into the following chapters.

Chapter 2 discusses the theoretical principles of laser cooling and trapping and evaporative cooling and summarizes the important properties of ^{23}Na relevant for laser cooling and trapping. It also gives an overview on important aspects of spinor BEC.

Chapter 3 gives a description of the experimental apparatus. This includes the vacuum system, the Na oven, Zeeman slower, magnetic coils and laser systems.

Chapter 4 describes the imaging system used to measure atom numbers and densities. The chapter includes the theoretical background and the experimental setup

for the absorption imaging system that I implemented.

In Chapter 5, the optimization of the cooling sequence is discussed in detail. I show how time of flight absorption imaging is applied to retrieve the atom number and temperature at various stages in the cooling sequence, and which parameters led to the highest numbers and smallest temperatures.

Chapter 6 ends with the conclusions and an outline of future planned experiments.

Chapter 2

Theoretical Background

2.1 Introduction

In this chapter I provide the theoretical background on laser cooling and trapping and evaporative cooling that is necessary for the realization of Bose-Einstein condensation in cold atomic gases. The chapter begins with a description of the methods of laser cooling and trapping, Zeeman slowing and the physical properties of sodium as they relate to laser cooling. The chapter ends with a section where I describe the basics of a spinor BEC as future planned experiments will be on cold collisions in sodium spinor BECs.

2.2 Laser Cooling and Trapping

When an atomic beam interacts with a counterpropagating red-detuned laser beam, photons are absorbed and momentum exchange takes place. Photons are absorbed from a certain direction, but they are re-emitted by the atoms in random directions due to the spontaneous emission. A net force results that causes a deceleration of the atoms over many cycles. The absorption and re-emission of many photons reduces the kinetic energy of the atoms. So, if we use pairs of red-detuned counterpropagating laser beams and interrogate atoms from all six directions along the cartesian axes, then the kinetic energy along each dimension will be reduced. The slowed atoms will have a lower temperature and more narrow velocity distribution as the average kinetic energy of the atomic cloud is reduced. This principle is at the heart of laser cooling [7].

The absorption of photons by the atoms shows a strong frequency dependence. The absorption profile is a Lorentzian line centered at the Doppler-shifted resonance

frequency. This frequency dependence is translated to velocity dependence by the Doppler shift. Due to the Doppler effect, atoms most strongly interact with the cooling beams that oppose their velocity direction. Therefore, three orthogonal pairs of counterpropagating red-detuned laser beams are used to decelerate the atoms moving in any direction. The resulting scattering force is a velocity-dependent dissipative force, acts like a friction force, and is used in laser cooling to cool down the atoms. The excess energy of the atoms after cooling is carried away by the re-emitted photons. The limit to this cooling is reached when the random walk due to spontaneous emissions, which causes heating, is balanced by the cooling effect of the scattering force. The resulting temperature is known as Doppler temperature. It is given by

$$T_D = \frac{\hbar\Gamma}{2k_B},$$

where Γ is the Lorentzian linewidth of the atomic transition,

$$\Gamma = \frac{1}{\tau},$$

and τ is the lifetime of the excited state. For alkali atoms, T_D is typically on the order of ~ 100 μK. This is known as optical molasses [8].

The optical molasses decreases the temperature of the atoms in the overlap region of all laser beams by reducing the average kinetic energy of the atoms, but it does not provide a spatial confinement for the atoms. The atoms slowly move out of the laser beam region because of diffusion at the Doppler temperature. To provide a spatial dependence and create a trap, we use the magneto-optical trap (MOT), a technique which combines both the cooling lasers and magnetic fields to cool and trap the atoms simultaneously. The first successful demonstration of a MOT for neutral atoms was done by Raab in 1987 [9] but today it has become one of the most common traps to study cold neutral atoms.

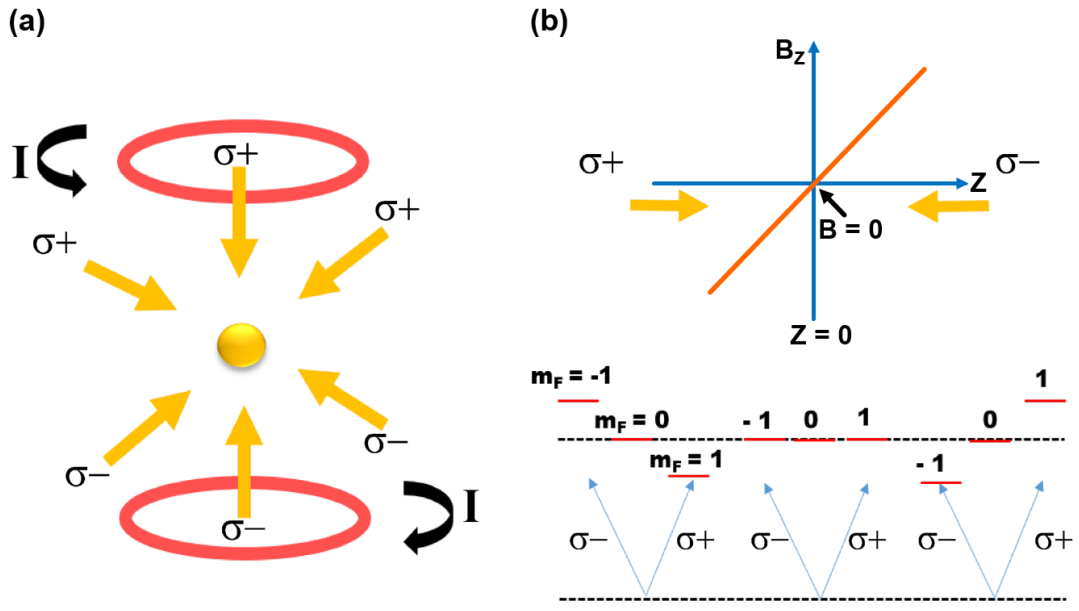

Figure 2.1: (a) Schematic diagram of a MOT with six laser beams and two coils in anti-Helmholtz configuration. The coils produce a quadrupole magnetic field that is zero between the two coils. (b) Schematic diagram of spatial Zeeman splittings and preferred absorption of different polarized beams at different positions.

The spatially varying radiation force in a MOT cools the atoms and traps them at the center with the help of an inhomogeneous magnetic field. The applied magnetic field is linear and is zero at the center. This quadrupole magnetic field gradient is achieved with coils in anti-Helmholtz configuration as shown in Fig. 2.1(a). The spatially-varying magnetic field creates spatially-varying Zeeman shifts of the hyperfine sublevels of the atoms as shown as cartoon in Fig. 2.1(b). Also shown in Fig. 2.1(b), the polarizations of the counterpropagating cooling beams are adjusted to be right and left circularly polarized. The polarizations are chosen so that the light pointing towards the center will interact more strongly with the atoms that are displaced from the center confining towards the beam, because their Zeeman shift brings those atoms

closer to resonance. Due to this position-dependent interaction, the atoms are pushed towards center of the trap like a mass tied to a spring. The resulting force is a restoring force that combines with the cooling/dissipation force from the optical molasses. The atoms are both cooled and compressed towards the center. This is the basic principle of the magneto-optical trap.

2.3 Zeeman Slowing

Before the thermal atomic flux from the oven can be trapped and cooled down to a lower temperature in the MOT, a different technique called Zeeman slowing is used to slow and precool the hot atoms. It is used to reduce the velocity of a large flux of hot atoms at v $\sim 700\ \frac{m}{s}$ to the MOT capturing velocity of v $\sim 20\ \frac{m}{s}$ so that large number of atoms can be captured by the MOT [10, 11]. There are several types of slowers that can be used to slow down the atoms and increase the capture efficiency of atoms into the MOT [10, 12, 13, 14, 15].

The flux of slowed atoms and final velocity depends upon the power and the detuning of a Zeeman slower laser beam that counterpropagates along an atomic beam with a typical length of ~ 1 m. In all Zeeman slowers, a counterpropagating laser beam is used to decelerate the atoms via momentum transfer due to absorption. However, as the atoms are in motion, it is necessary to overcome the changing Doppler effect during the deceleration to slow down a large number of atoms. There are various methods which can be used to compensate the Doppler effect such as varying the laser frequency by the frequency chirp method [16], using broadband lasers [17] or by using a spatially varying magnetic field [10, 12, 14, 18, 19, 20, 21, 22] as shown in Fig. 2.2, generated by a tapered solenoid wrapped around the atomic beam tube, together with a fixed-frequency slowing laser. We use a spatially varying magnetic field for our slower.

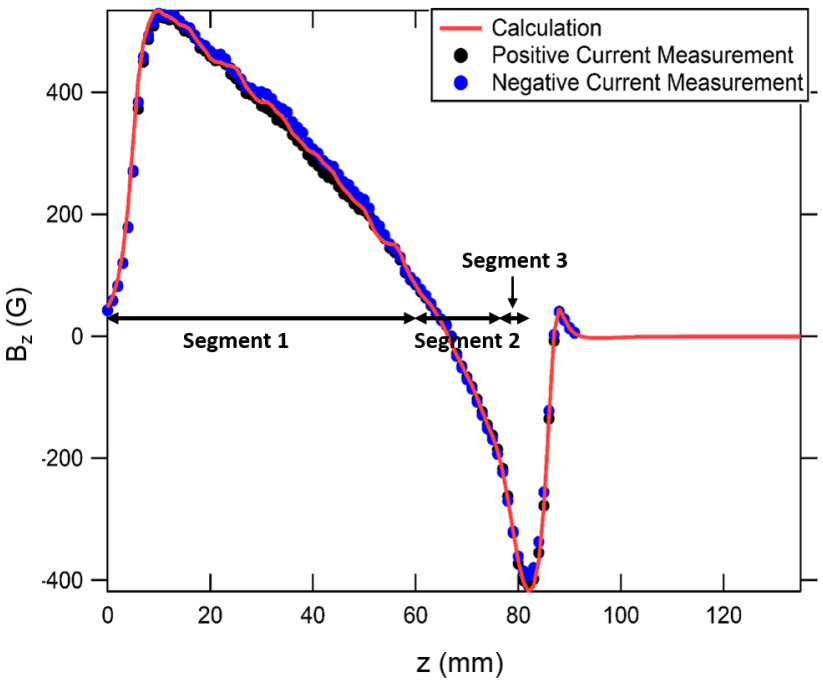

Figure 2.2: Plot of the longitudinal magnetic field component as a function of longitudinal position along the Zeeman slower in our lab. The field is generated by a tapered solenoid. The data points correspond to Hall probe measurements, the solid line is the result of a numerical simulation.

2.4 Atomic properties of Sodium

The atomic properties of alkali atoms make them more preferable for laser cooling and trapping experiments compared to other elements. These atoms have isolated, strong atomic transitions, that are easily accessible using diode laser systems or dye lasers and therefore are good candidates for laser cooling experiments.

Rubidium atoms are the first alkali atoms that were condensed into a BEC in 1995 [4]. However, for our experiment we are using sodium atoms and cool on the atomic transition of the D_2 line $3^2S_{\frac{1}{2}} \longrightarrow 3^2P_{\frac{3}{2}}$, which has a wavelength of 589.158 nm as shown in Fig. 2.3. We use F to denote the ground state manifold, $3^2S_{\frac{1}{2}}$ and F' to

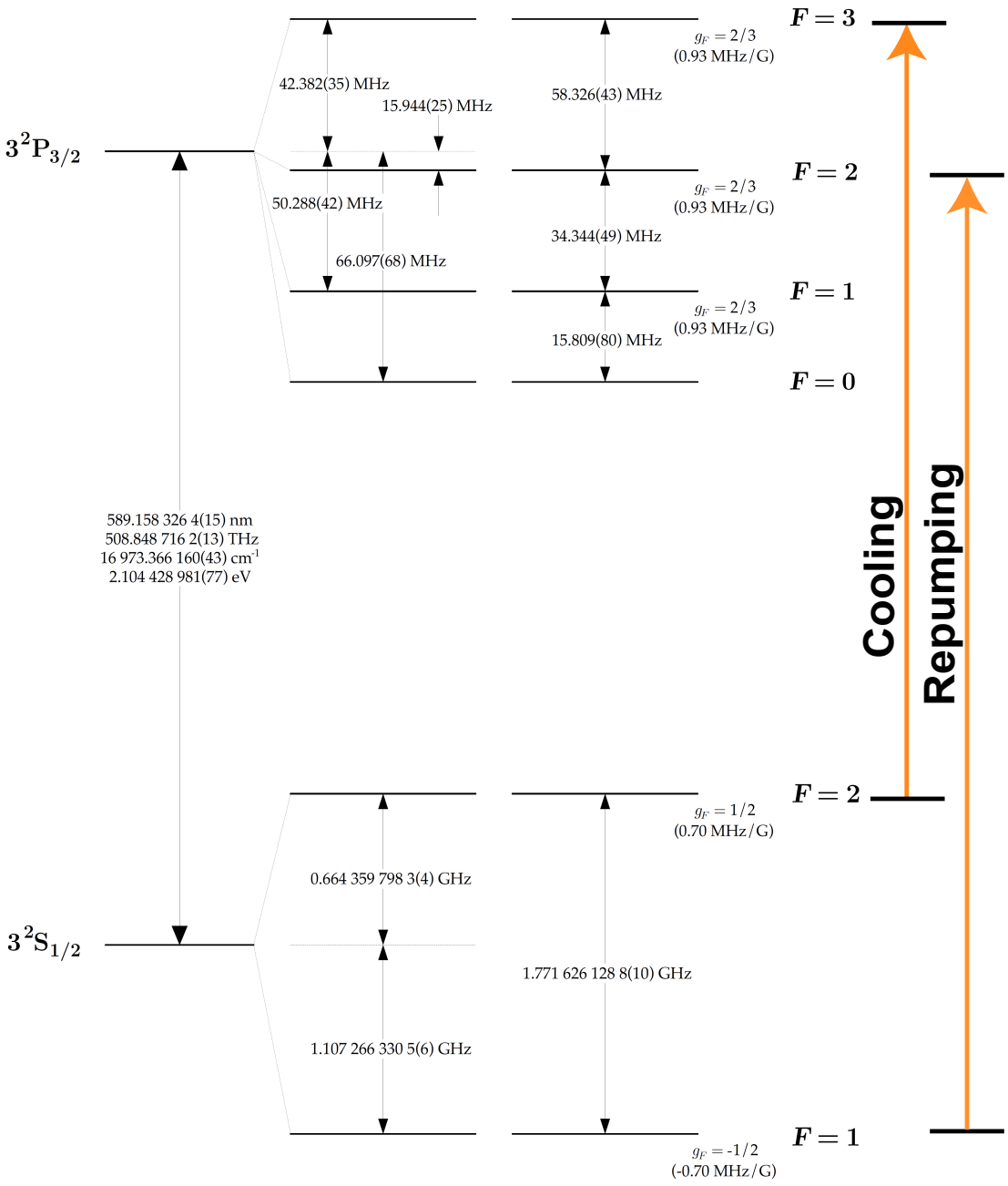

Figure 2.3: Energy level diagram of the D_2 Line of sodium with all the hyperfine splittings of the $3^2S_{\frac{1}{2}}$ ground state and $3^2P_{\frac{3}{2}}$ excited state, reproduced from [1]. F is the total angular momentum. The cooling transition F= 2 $\longrightarrow$ F'= 3, and the repumping transition F= 1 $\longrightarrow$ F'= 2 are highlighted.

refer to the excited state manifold, $3^2P_{\frac{3}{2}}$.

The closed atomic transition F= 2 $\longrightarrow$ F'= 3 is used for laser cooling for the creation of the MOT. The natural linewidth of the D_2 line is $\Gamma = 2\pi \times 9.795$ MHz and the hyperfine splitting between F'= 2 and F'= 3 is 58 MHz. Although the laser linewidth is only on the order of 1 MHz, the possibility of off-resonant transitions from F= 2 $\longrightarrow$ F'= 2 is non-negligible. Any atom in F'= 2 can decay to the F = 1 state, which is a dark state, and be lost from the cooling cycle. For this reason, we need a repumper laser beam resonant with F= 1 $\longrightarrow$ F'= 2. The repumper can then excite all the atoms back to F'= 2 state and keep the atoms in the cooling cycle.

2.5 Evaporative Cooling

In the MOT, when employing optimized sub-Doppler cooling methods (see chapter 5), atoms can be cooled to μK temperatures. But for the final cooling to reach nK temperatures atoms are transfered to a far off resonant optical trap (dipole trap) [23], formed by the focus of an infrared laser beam. The dipole force creates a position-dependent light shift and pushes atoms to the center of the beam focus. In the dipole trap, the atoms are not absorbing and re-emitting photons anymore. The heating due to spontaneous emission is therefore avoided. Evaporative cooling is then applied to reach BEC. Evaporative cooling is based on the principle of removing atoms with higher-than-average kinetic energy from the trap by lowering the depth of the trapping potential by lowering the dipole trap beam power [23]. Using this method, the most energetic atoms escape the trap and remaining atoms thermalize because of energy exchange during collisions. This technique can reduce the temperature of the cloud to $\sim$ 100 nK at the expense of loosing $\sim$ 90% of all the atoms, while retaining high densities $\sim 10^{14}$ cm^{-3} as needed to reach BEC.

2.6 Bose-Einstein Condensate (BEC)

It took 70 years for the experimental realization of Bose-Einstein condensates in ultracold gases [4, 5]. The theory was predicted and developed in 1924 by Satyendra Bose for photons [24]. Albert Einstein, in 1925, found that this theory can be extended and applied to bosonic atoms [25]. Einstein found that below the transition temperature, macroscopic numbers of bosonic particles occupy the ground state as shown in Fig. 2.4. Those particles form the BEC, which occurs when the temperature is low enough and the density is high enough for the inter-atomic separation to be less than the de Broglie wavelength, $n\lambda^3_{dB} > 2.612$, where n is the particle density and λ_{dB} is thermal de Broglie wavelength.

In the region of the condensate, all atom have identical wave functions which start overlapping to produce one macroscopic wave function, as shown in Fig. 2.4. In other words, for a BEC consisting of N atoms, the total many-body wave function factorizes into a product of N identical single-particle wave functions. In 1997, S. Chu, C. Cohen Tanoudji and W. Phillips won the Nobel prize for their work on the exploration of sub-Doppler laser cooling [9, 26, 27]. The development of laser cooling and the realization of BEC using laser cooling and trapping gave rise to a whole new field of experimental physics. In 2001, E. A. Cornell, W. Ketterle and C. E. Wieman were awarded the Nobel prize for the realization of BEC in dilute alkali atom gases. And over the years, many condensates have been realized for different elements such as ^{7}Li [28, 29], ^{85}Rb [30], ^{39}K [31], ^{133}Cs [32], ^{52}Cr [33], ^{40}Ca [34], ^{84}Sr [35], ^{164}Dy [36] and ^{168}Er [37]. BEC in hydrogen was also obtained after the development of an evaporative cooling method in 1998 [38].

In this thesis, experimental work towards matter-wave quantum optics in spin space with sodium spinor F= 1 BEC will be discussed. The next section discusses the experimental importance of F = 1 spinor BEC.

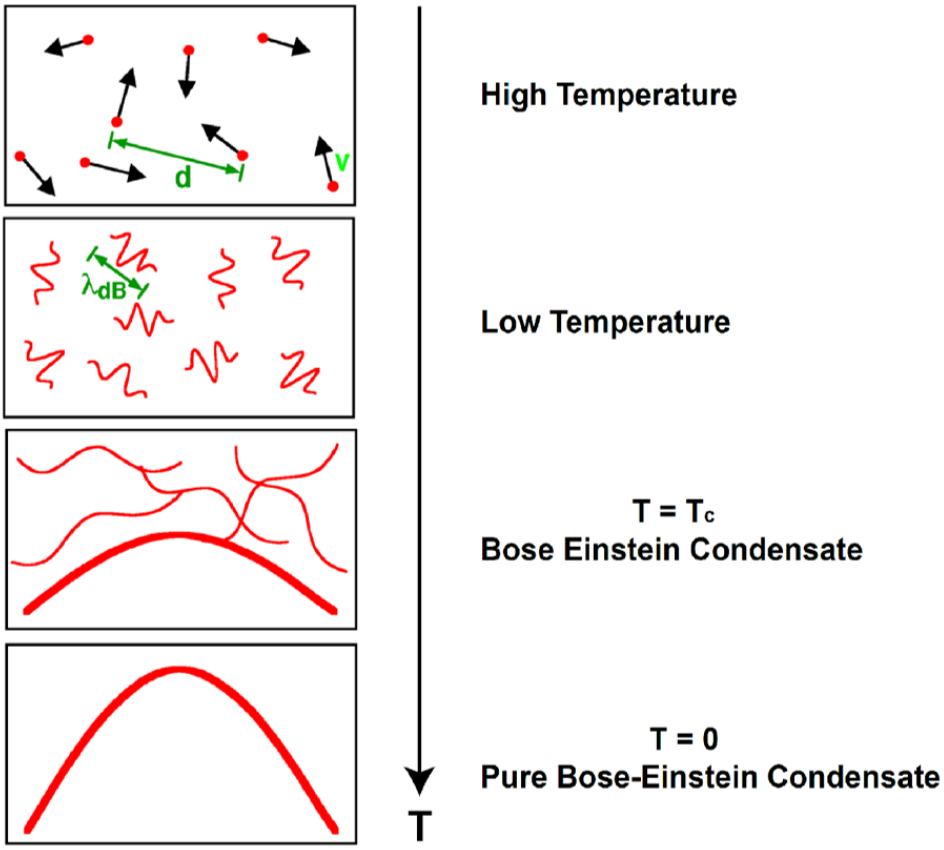

Figure 2.4: Cartoon showing the BEC transition. A BEC starts forming when $T = T_c$. In the condensate, all atoms have identical wave functions. When the temperature is decreased to absolute zero, a pure BEC with one macroscopic wave function is formed. Drawn after [2].

2.7 Spinor BEC

In the early years of BEC research, only single-spin-component BECs of Rubidium (^{87}Rb) [4], Sodium (^{23}Na) [5] and later Lithium (^{7}Li) [29] were created by using magnetic traps that trapped only one Zeeman sub-level of the ground state. However, a new domain for the research in ultracold atoms was established with the first realization of spinor BEC in 1998 in a gas of ^{23}Na spin-1 atoms [39]. The atoms were confined in an optical trap and changes in their spin directions were observed

because of the interaction between the atoms. Later, all-optical methods to create spinor BECs and observe richer spin dynamics were developed [40]. In such a trap, BEC with spin-F gives rise to a mixture of spin textures [6] as it has 2F + 1 spin components varying over space and time. A scalar quantity like a single spin BEC component in a magnetic trap will lack these interesting textures and dynamics.

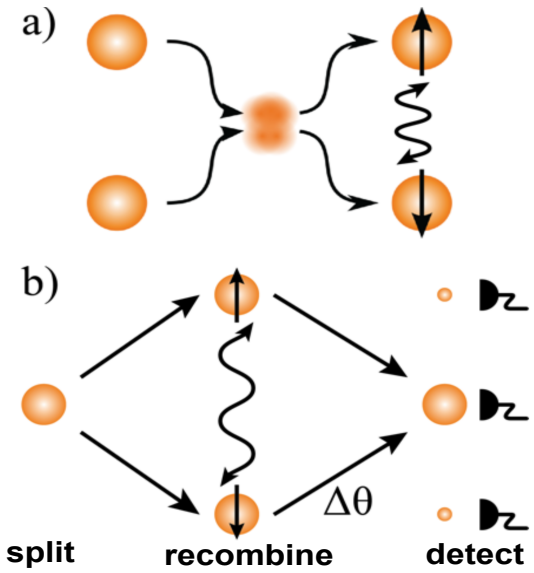

Figure 2.5: (a) Cartoon of four wave mixing with spin-changing collisions in (^{23}Na) atoms. (b) Inferometry sequence with collisions where $\Delta\theta$ is a phase-shift applied via microwave-dressing of the F = 1 $\longrightarrow$ F' = 2 transition. The wavy line illustrates creation of an entanglement and two mode squeezing. Up arrows denote magnetic number m_F = + 1, down arrows denote m_F = - 1 and missing arrows denote m_F = 0.

F = 1 spinor BEC dynamics are fascinating and there are many groups around the world who are studying those dynamics such as spin waves [41], spin dynamics [40] and a new type of squeezing called spin-nematic squeezing [42]. Recently, the group of M. Oberthaler in Heidelberg found that the precise control of collisional energies with microwaves allows quantum interferometry using matter-wave quantum optics in spin space with Rb, which is ferromagnetic [43]. Our group is studying the spin exchange

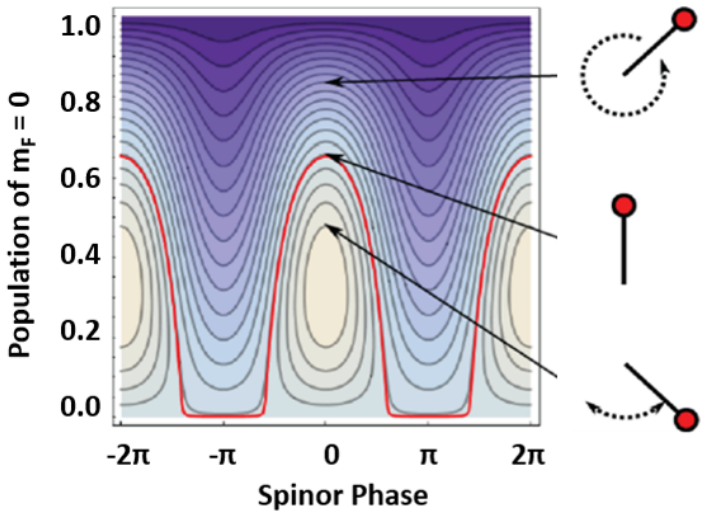

Figure 2.6: The phase-space diagram of ^{23}Na. Colors corresponds to the energy of the system, brighter color corresponds to the higher energy. Lines are equal energy contours. An analogy to pendulum motion is shown on the right.

collisions in F = 1 ^{23}Na spinor BEC to do experiments on quantum interferometry in the anti-ferromagnetic spinor BEC, as illustrated in Fig. 2.5. The system evolves differently for anti-ferromagnetic and ferromagnetic spinor BEC. The higher energy region shown in the phase-space diagram for Na in Fig. 2.6 will become a low energy region for Rb and therefore, will result in a different interference fringe pattern at the output of interferometer sequence.

For F = 1 spinor BECs the spin interaction parameter c_2 categorizes whether the collisional coupling is ferromagnetic or anti-ferromagnetic [44]. It is defined as [45]

$$c_2 = \frac{4\pi\hbar^2}{m}\Delta a, \tag{2.1}$$

where m is the mass of the atom, $\hbar$ is Planck's constant and $\Delta a = (a_2 - a_0)/3$ is the scattering length difference between the s-wave $F_{tot} = 2$ and s-wave $F_{tot} = 0$ collision channels. When $(a_0 > a_2)$ the collisional coupling is ferromagnetic and when $(a_0 < a_2)$ the collisional coupling is anti-ferromagnetic [44]. Therefore, a ^{23}Na F= 1 spinor BEC

is anti-ferromagnetic [46, 47] and a ^{87}Rb F = 1 spinor is ferromagnetic [48, 49]. The resulting spin dynamics are quite different and warrant detailed study for each case. In order to study processes such as those shown in Fig. 2.5 in sodium we first need to apply laser cooling and trapping to create an ultracold gas. This is described in the next chapters.

Chapter 3

Cooling and Trapping System

3.1 Introduction

In this chapter, I briefly describe the experimental setup we have built to soon achieve a sodium spinor BEC in our lab. There are several steps that are followed towards reaching the BEC. At first, the hot and fast moving sodium atoms out of an oven are slowed down in a Zeeman slower. Then, by using a cooling laser system and magnetic fields, they are trapped and cooled down in an ultra-high vacuum chamber. In the future, forced evaporative cooling methods will be used in a dipole trap to lower the temperature of the ultracold atomic cloud to low temperatures of ~ 100 nK, starting from a temperature of ~ 700 μK in the MOT. Here, I will briefly go over the apparatus that I worked on that is used for the first step of the BEC experiment to create a magneto-optical-trap (MOT). When I joined the research group, there was a pre-existing setup of a vacuum system as shown in Fig. 3.1(a) and a cooling and re-pumping laser system as shown in Fig. 3.6, but there was no MOT.

3.2 Experimental Setup

This section contains a general a description of the vacuum apparatus that is used to achieve a low pressure of $p < 10^{-10}$ Torr in the main experimental vacuum chamber. A low pressure is needed to minimize loss of trapped atoms and heating due to collisions with hot background gas atoms. In this section, I also provide the details of the best oven temperature values that generate a large sodium atom flux from the oven while retaining low pressure, and the optimum current values of different segments of the Zeeman slower. Finally, I also discuss the framework of precise control of the magnetic

field and field gradient to achieve zero field at the center of the experimental chamber.

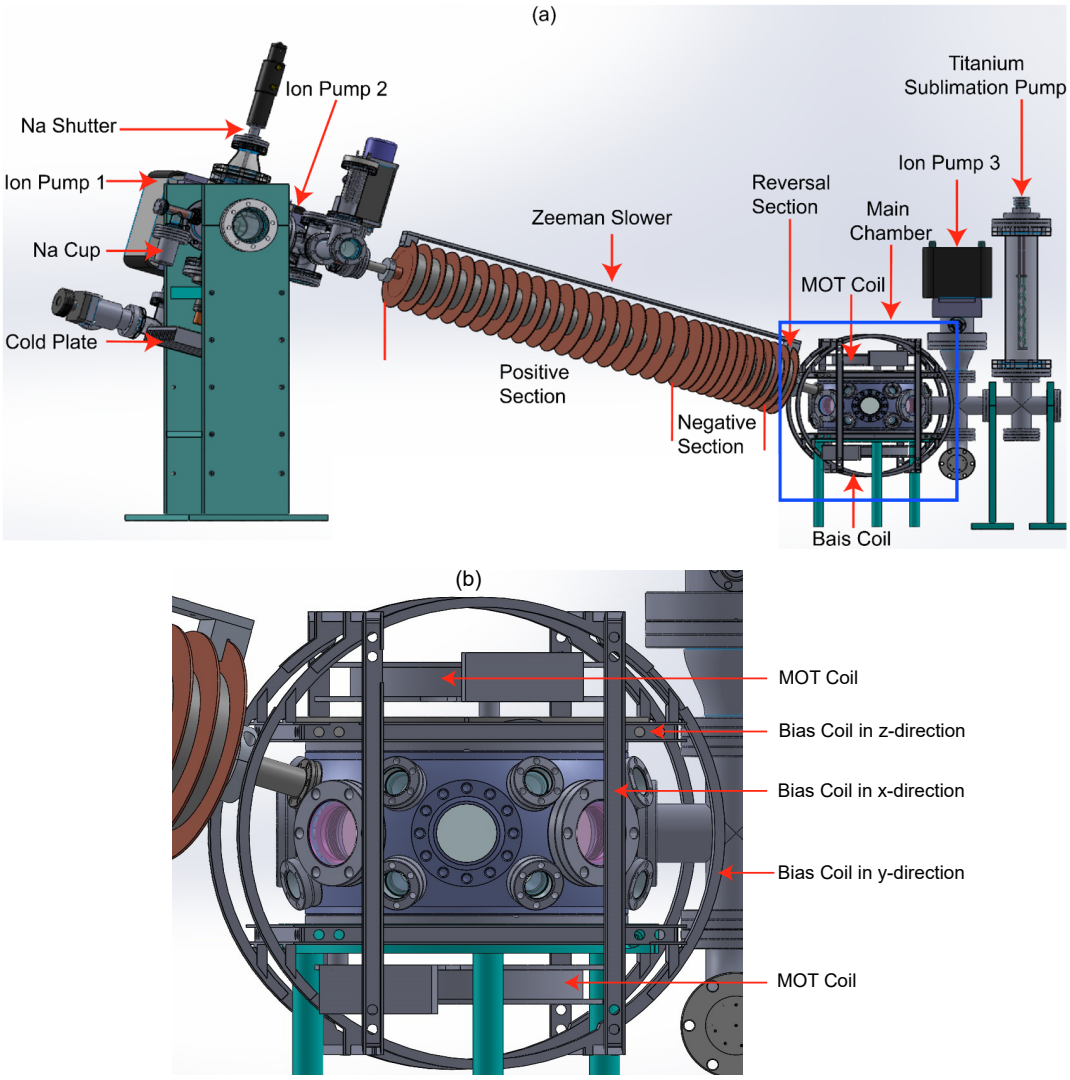

Figure 3.1: (a) CAD rendering of the ultra high vacuum system. (b) Close up of the blue outlined region in (a), showing the main vacuum chamber where the ultracold atomic cloud is formed. The chamber is surrounded by low current (5 A) bias Helmholtz coil pairs and high current (80 A) anti-Helmholtz coils. The anti-Helmholtz coils are built on the top and bottom of chamber. The three pairs of Helmholtz bias coils are held along the x, y and z directions of the chamber.

3.2.1 Vacuum System

The experiment is carried out in a stainless steel ultra-high vacuum chamber (UHVC, Kimball Physics 8" extended spherical octagon). The chamber is maintained to be at low pressure of $< 10^{-10}$ Torr so that the atoms in the trapped cloud do not collide often with hot background gas atoms. Such background collisions reduce the trap lifetime, reduce the total number of atoms in the trap, and increase the temperature. It is difficult to achieve such a low pressure when the high temperature Na oven is connected directly to the system, because the oven chamber usually operates at p $\sim 10^{-8}$ Torr.

A differential pumping chamber is therefore connected between the oven and the main chamber to provide an increased pressure gradient. The differential pumping chamber is connected to the oven via a narrow custom-made 0.3 inch diameter and 5 inch long stainless steel tube welded onto a double-sided CF flange and to the Zeeman slower via a similar tube.

Each part that is connected to the vacuum chamber, as well as the vacuum chamber itself, is continuously pumped on with ion pumps to maintain low pressures. Altogether, there are three 50 $\frac{l}{s}$ ion pumps (Duniway DSP-OSO-5125-M). The first ion pump is near the oven, the second one is near the differential pumping chamber and the last ion pump is connected to the main experimental chamber. They maintain the pressure of 10^{-8} Torr, 10^{-9} Torr and 10^{-10} Torr in the oven, the differential pumping chamber, and the main chamber respectively. There is also one titanium sublimation pump which is connected to the main chamber. When the filament of this pump is heated for 20 minutes, it sputters titanium onto the nearby metal surfaces. This Ti layer absorbs gases present in the vacuum system.

An angle valve is connected to the ion pump at the oven chamber. It is used for rough pumping with a portable pumping station that contains a turbo pump and a

mechanical pump (Pfeiffer HiCube 80 Eco). The angle valve is also used to backfill the system with dry nitrogen if necessary.

3.2.2 Oven

The initial stage of the experiment begins from the stainless steel oven. A large flux of sodium atoms is generated from the oven by heating up the reservoir to 345 °C. The reservoir consists of a 2.75" Conflat stainless steel cup. The cup is filled with a 5 g prescored sodium ampule (Strem Chemicals 93-1020.5) that is broken under air just before loading the oven, a few minutes before pumping. An oven nozzle forms a collimated atomic beam. The oven nozzle is made out of copper, is 1.7 inch long and has a 0.7 inch outer and 0.24 inch inner diameter. The front and the back of the oven nozzle are heated up to 415 °C as this temperature is sufficient to avoid the deposition of sodium atoms inside the nozzle tube. The nozzle is thick to maximize the ratio of volume to surface and therefore minimize radiative heat loss in the vacuum environment. The oven and nozzle temperatures are actively stabilized using commercial PID temperature controllers (Automation Direct S4848-CR and Avatar CIP-12-20) connected to flange heaters on the cup and on the nozzle flanges (Tempco MPP51101, MPP02838, MPP52501).

After several months sodium atoms start to deposit on one of the oven windows and on the 1.33" CF viewport on the main chamber opposite the Zeeman slower tube. The accumulation of atoms on the main chamber viewport hinders the Zeeman slowing as this viewport is used by the laser beam that slows the atomic beam. This in turn slows down the loading of the MOT and also decreases the atom number in the MOT. The accumulation of atoms on the oven window makes it difficult to see the nozzle opening for visual diagnostics. Therefore, we shine UV light from LED sources (LED Engin LZ1-UV00-0000 1.2W LED @ 365mm) onto those windows to

desorb those deposited atoms. This technique is better than other techniques as it helps to maintain the low pressure in chamber and oven [50] and can be performed without breaking vacuum.

A custom copper cold plate in the oven chamber is connected to the air side with a thick copper feedthrough and cooled to -12 °C using a water-cooled array of TEC elements (6* TEC1-12706). The cold plate collects hot Na atoms that exit the nozzle at larger angles and prevents those atoms from increasing the Na background pressure in the oven chamber. A hole with 0.25" diameter in the center of the cold plate allows atoms from the center of the beam to pass through into the differential pumping tube and through the differential pumping chamber into the Zeeman slower tube. A pneumatic shutter behind the cold plate allows us to mechanically switch the atomic beam on and off.

3.2.3 Zeeman Slower

The first stage of cooling is done in the Zeeman slower. The large flux of atoms coming out of the oven is slowed and pre-cooled by the Zeeman slower via a counterpropagating laser beam which is red-detuned by several hundred MHz with respect to the atomic transition. There are three computer-controlled power supplies (Extech DCP60) that are used to adjust the magnetic field gradient in the Zeeman slower. These power supplies are referred to as segment 1, segment 2, and segment 3, and are designed to perform with a current of 4 A. Segment 1 is the power supply used for the positive section, segment 2 for the negative section and segment 3 for the reversal section of the Zeeman slower as shown in Fig. 2.2 and Fig. 3.1(a).

The tapered solenoid surrounding the Zeeman slower is divided into 30 sections that are interspersed with copper discs to allow effective passive cooling of the sections. The magnetic field gradient created by the solenoid causes a position-dependent Zeeman

shift that compensates the changing Doppler shift as atoms are decelerated on their way down the tube. The Zeeman slower is designed to slow atoms from 700 $\frac{m}{s}$ down to 20 $\frac{m}{s}$ so they can be captured by the MOT.

3.2.4 Experimental Chamber

The stainless steel experimental chamber has eight 2.75" CF viewports, four of which are used for the MOT cooling and repumping beams, and two of which are used for sideways imaging. It also has sixteen 1.33" CF ports, two of which are used for the Zeeman slower atomic beam and Zeeman slower laser beam, and two of which are used for electrical feedthroughs to connect to two homebuilt antennas inside the chamber. One antenna is a loop RF antenna for frequencies of 50 kHz - 1 MHz to excite transitions between the F = 1 magnetic sub-levels. The other antenna inside the chamber is a homebuilt quarter-wave monopole antenna for frequencies around $\sim$ 1.8 GHz to excite F = 1 $\longrightarrow$ F = 2 transition between the two ground state hyperfine manifolds. The chamber also has two 8" CF viewports used for MOT beams and top-down imaging.

3.2.5 Field Control

To create the MOT in the main experimental chamber, we need magnetic field gradients and laser beams. The laser system is discussed in detail in section 3.3. Here, I will describe the magnetic field control. Constant stable magnetic fields and field gradients are very important not just for the MOT but also for our future experiments, as our experiments are based on the rate of spin-changing collisions in the ultracold cloud. The collision rate depends on the quadratic Zeeman effect ($\sim$ 700 $\frac{Hz}{G^2}$ compared to a collision energy of $\sim$ 30 Hz) which shifts the energy levels of pairs of atoms with magnetic quantum number $m_F = 0$ and pairs of atoms with $m_F = \pm 1$. Therefore,

we need good control of the magnetic field on the level of 100 mG over the region of space that contains the atomic cloud.

(i) MOT Coils

For our experiment, we use a pair of water-cooled anti-Helmholtz coils (MOT coils) to create the quadrupole field for the MOT, as shown in Fig. 3.1(b). These coils are placed on the top and the bottom of the chamber along the z-axis and have a diameter of 140 mm and thickness of 178 mm. The insulated copper tubing used has an outer diameter of 3.18 mm and inner diameter of 1.8 mm. With the cooling water at 30 °C and 20 windings of copper tubing, we are able to reach a current of 82 A. These coils provide a maximum quadrupole field of 12 G/cm gradient at the center of our chamber, sufficient to create a strong compressed MOT.

(ii) Bias Coils

The earth's magnetic field and field from the ion pump magnets near the chamber have some effect at the center of the chamber. Therefore, to provide a zero field at the center of the chamber, we use three pairs of bias coils in Helmholtz configuration. By changing any magnetic fields at the center of the chamber, the trapping is controlled and we are able to center the MOT and keep the MOT centered as the Zeeman slower magnet is switched on or off. Each coil pair is different in shape and size, shown in Fig. 3.1(b). Bias coils in the z-direction are square with side length of 235.5 mm and provide 3 G at 5 A at the chamber center. The coils in the x-direction are also square but have a length of 275 mm and provide 5 G at 5 A. Lastly, the coils in the y-direction are circular in shape with diameter 294 mm and provide 5 G at 5 A. They all use 33 windings of copper wire

and work within the range of ± 5 A. The coil frames were 3D printed using the 3D printing studio in the University of Oklahoma library.

(iii) Noise Reduction in Bias Coil Current Control

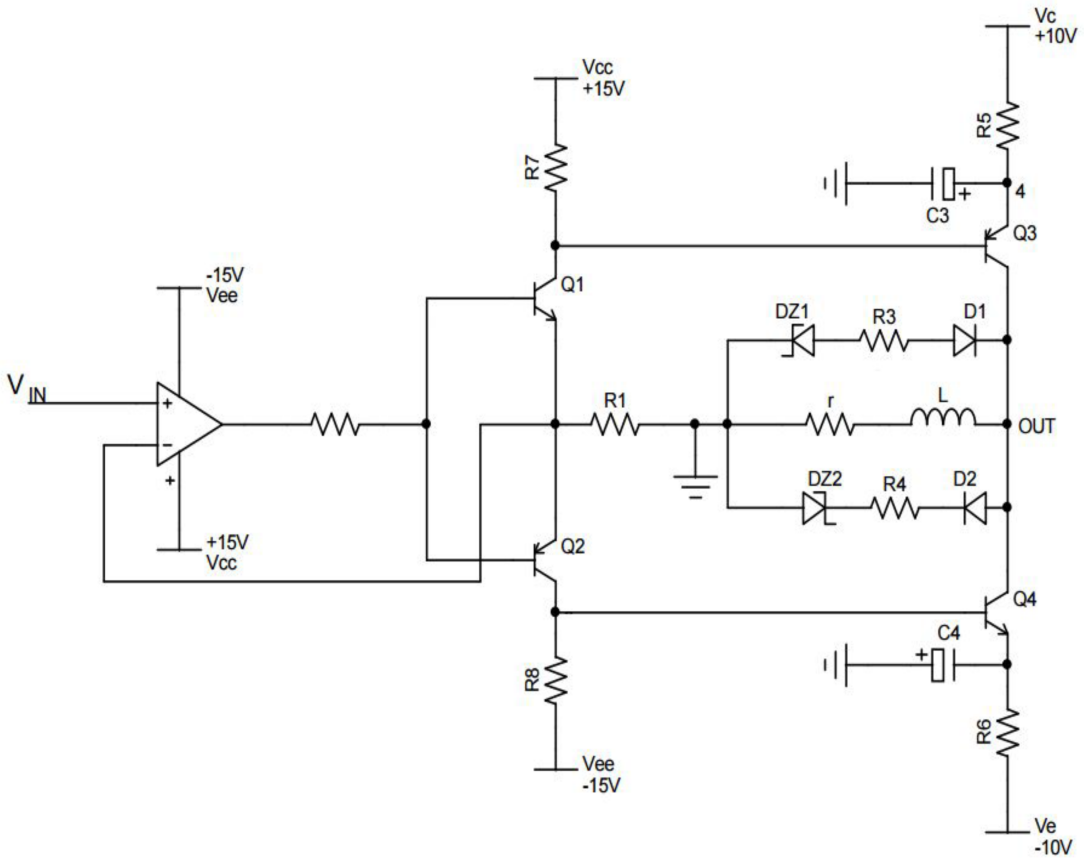

Figure 3.2: Schematic of current control system for the bias coils. Q_1 and Q_2 are low power transistors, used to protect most of the circuit from the higher currents of up to 5 A that flow through the high power transistors Q_3 and Q_4. The operational amplifier is a high speed IC, initially chosen to allow switching within 10 μs. The input is provided by a homebuilt analog PI controller (not shown). The PI controller uses the voltage across a small sense resistor (0.1 Ohm) in series with each trim coil to sense the current and compare it with a setpoint given as an analog voltage by the experimental control computer. Reproduced from [3].

Stabilized bipolar current supplies/amplifiers were built in our lab to produce rapid current control of ± 5 A for all six bias coils. The schematic is shown in Fig. 3.2 and the photo of home-built supplies is shown in Fig. 3.3. For the fast switching, proportional and integral (PI) control was used in all supplies. Initially, large fluctuations were observed in the output signals.

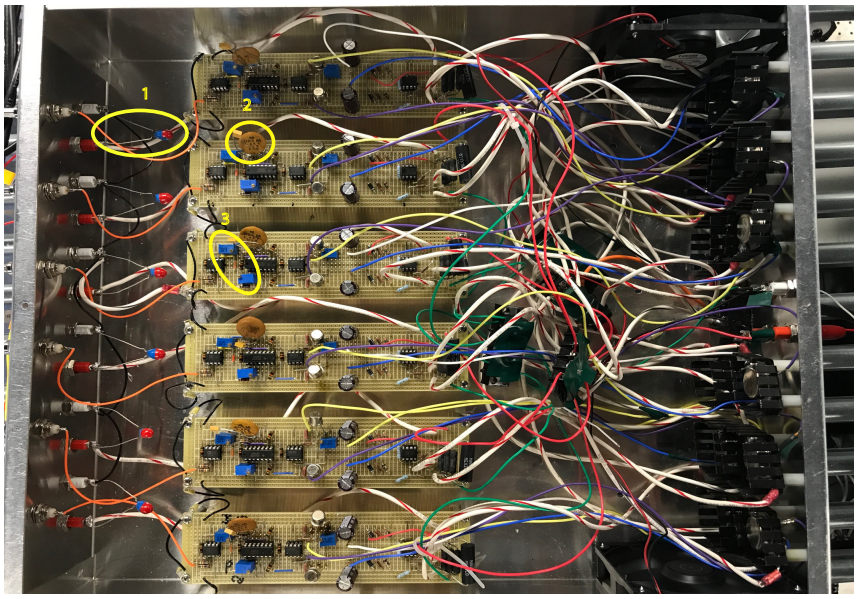

Figure 3.3: Photo of the homebuilt current control system for the bias coils. Output and gain filtering capacitors were added later to prevent oscillation and noise at the cost of slowing down switching speed from 10 μs to 1.5 ms.

To reduce the fluctuations, a 23 μF filtering capacitor was added in parallel with the output of each of the supplies and a 10 nF capacitor was added to adjust the gain range of the PI control loop as shown in Fig. 3.3. Further, potentiometers of both proportional and integral were changed empirically to prevent oscillation of the feedback loop for all setpoints and reduce the current noise. The addition of the filtering capacitors and changing of gain

potentiometers helped to increase the signal to noise ratio of the coil current but also increased the switching time from the design value of ~ 10 μs to 1.5 ms.

3.3 Laser Setup

Along with the ultra-high vacuum system and magnetic fields we also need a laser system to perform the laser cooling and trapping. The following section briefly discusses the laser setup used in our experiment.

3.3.1 Light Distribution

For the laser setup we use a frequency-doubled diode laser at 589 nm output wavelength with power P = 1.2 W (TOPTICA TA-SHG PRO). The laser beam is divided into two parts at the output. The first part is directed to a saturated absorption spectroscopy setup which is used to lock the laser. The second part is used to generate the cooling, slowing, and imaging beams and their respective repump beams to create and characterize the MOT.

The laser is locked 105 MHz to the red of the F = 2 to F' = 3 cycling transition. It is very important to actively lock the laser and cancel any frequency fluctuations and drifts which affect our experiments adversely. The stabilization of the laser frequency is influenced by factors like mechanical stress, vibrations of the table surface, temperature drift, electronic offset and laser alignment fluctuation.

Our laser is frequency stabilized using FM-modulated saturation spectroscopy. A Na vapor cell (Precision Glassblowing TG-ABNA, Pyrex, 25 mm OD $\times$ 75 mm path length) is heated to 120 °C and interrogated with a weak probe beam in the presence of a strong, counterpropagating pump beam. A double-passed 80 MHz Acoustic Optical Modulator (AOM) is used in the saturation absorption spectroscopy to modulate the

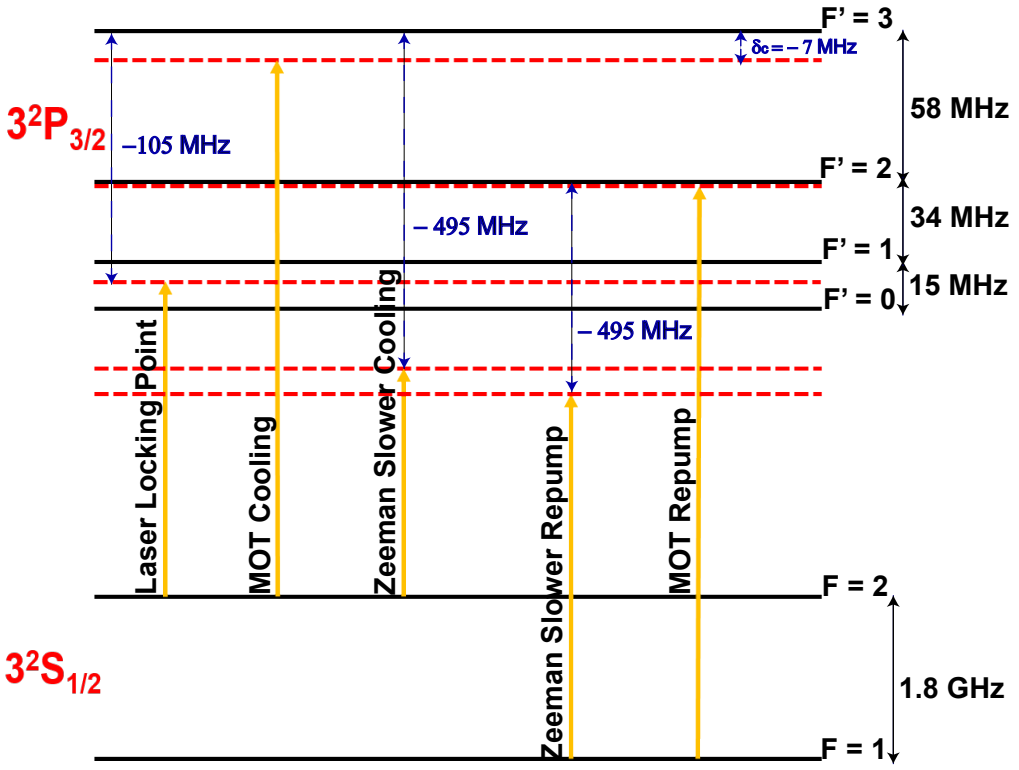

Figure 3.4: Frequencies of laser light used in the experiment compared to the hyperfine structure of sodium. Frequencies are not drawn to scale.

pump beam frequency and achieve a modulated pump-probe frequency difference of

$$\nu_{probe} - \nu_{pump} = \nu_o + \Delta\nu \sin(\omega_{ref}\, t)$$

with ν_o = 160 MHz, $\Delta\nu \approx 4$ MHz and $\omega_{ref} = 2\pi \times 30$ kHz. A lock-in amplifier monitors the probe absorption and generates an error signal proportional to the derivative of the Doppler free absorption Lamb-dips. The shifted laser is locked via a home-built analog PID circuit to the zero-crossing of the error signal corresponding to the F = 2 $\longrightarrow$ F' = 3 crossover peak. Therefore, the main laser system is locked at 105 MHz below F' = 3.

The frequency of the cooling laser is red-detuned with respect to the cooling cycle transition, δ_c = - 7 MHz during the MOT loading phase. In the past, researchers have also used the F = 1 $\longrightarrow$ F' = 0 transition to achieve a MOT, but the density of

such a MOT was lower [51, 52]. The Zeeman slower cooling beam is detuned to the red of the F = 2 $\longrightarrow$ F' = 3 resonance, -495 MHz below the F' = 3 state to compensate the large Doppler shifts in the atomic beam. Laser settings for all repumping beams used in the experiment are shown in Fig. 3.4.

Using the second part of the main laser beam coming out of the TA-SHG Pro, we generate the Zeeman slower laser beam discussed in section 3.2.3 and three orthogonal

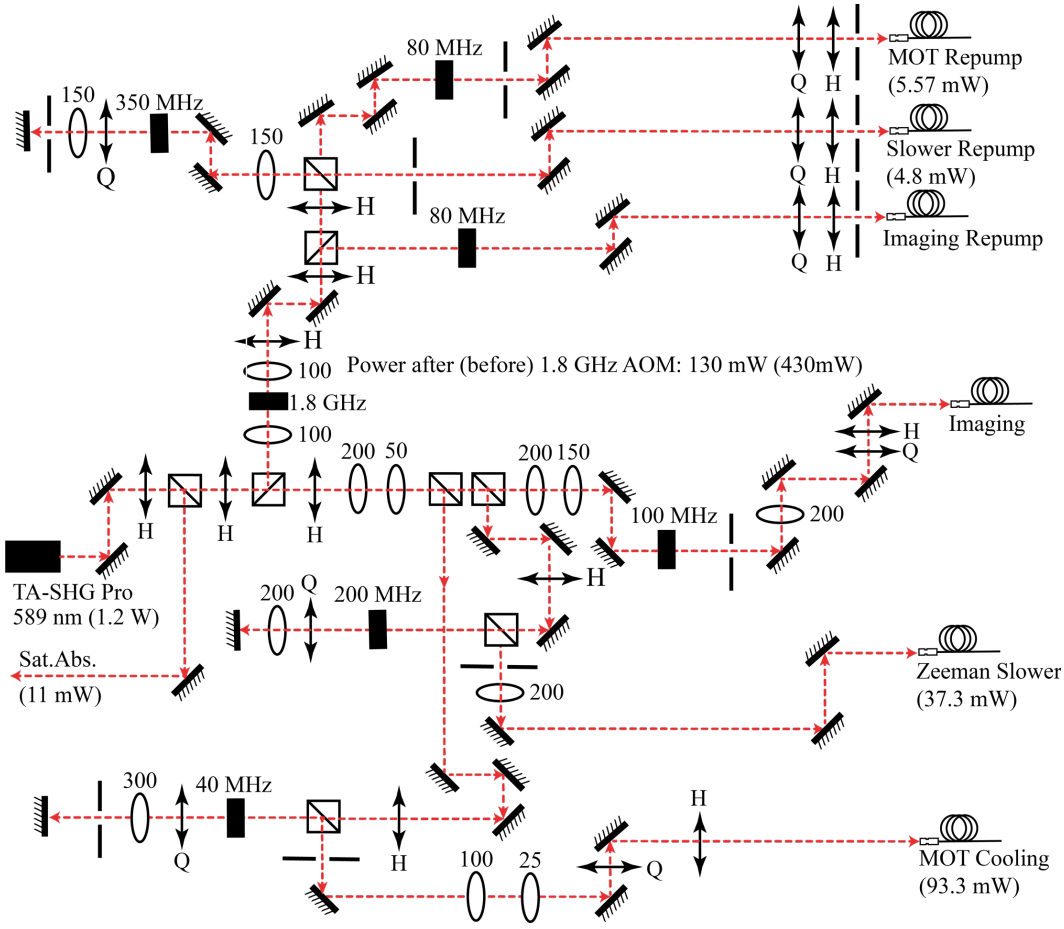

Figure 3.5: Schematic of the laser system used to generate cooling, repumping, imaging and Zeeman slowing beams. The abbreviations are AOM: acousto-optic modulator, Q: quarter wave plate, Sat. Abs: Saturation Absorption, H: half-wave plate, numbers: focal length in mm. All cubes are polarizing beamsplitter cubes. The last apertures shown before each fiber denote mechanical shutters.

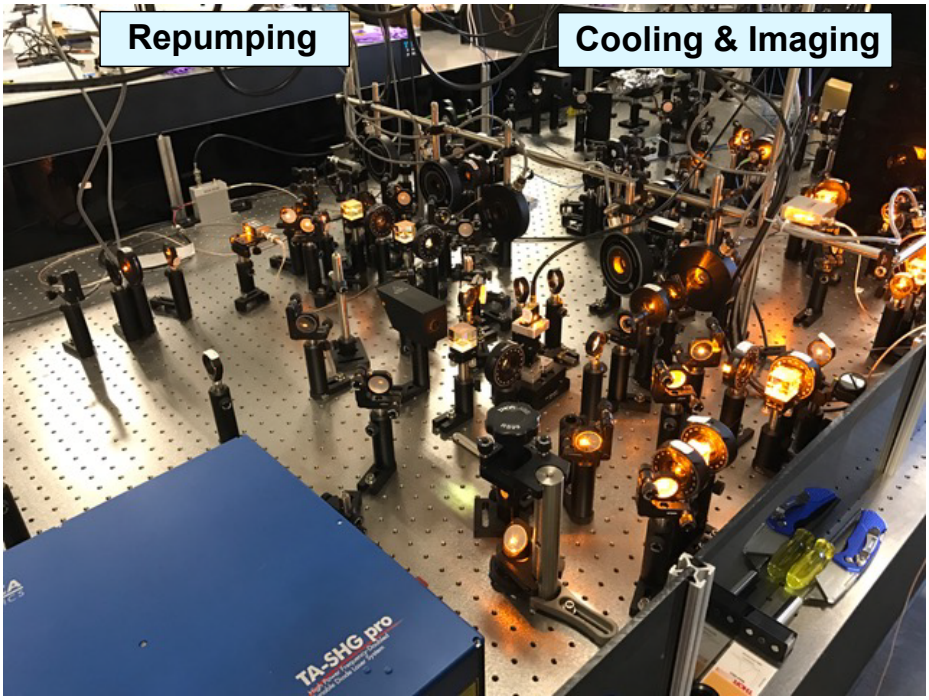

Figure 3.6: Photo of a part of the optics setup in our lab that was built to generate MOT, Zeeman slowing and imaging beams.

pairs of circularly polarized laser beams traveling in opposite directions referred to as MOT beams to create a MOT in the main experimental chamber. The MOT beams are red-detuned from the cycling transition for Doppler cooling [9]. Other than these beams we also generate the imaging beams to take images of the cloud, but these will be discussed in detail in chapter 4. All these laser beams have respective repumping beams which excite the atoms on the F = 1 to F' = 2 transition so that the atoms can be optically pumped back into the cooling cycle where they decay back to the F = 2 state instead of F = 1. Fig. 3.5 and Fig. 3.6 show the schematic diagram and the setup for the optics we have used to generate all those beams in our lab, using acousto-optic modulators to control frequencies and amplitudes and mechanical

shutters to completely shut off any beam as necessary. All the laser beams were setup on one 5' × 10' optical table and transfered to the experiment table using polarization maintaining optical fibers as it is easy to realign the beams on the laser table without affecting the beam paths on the experiment table.

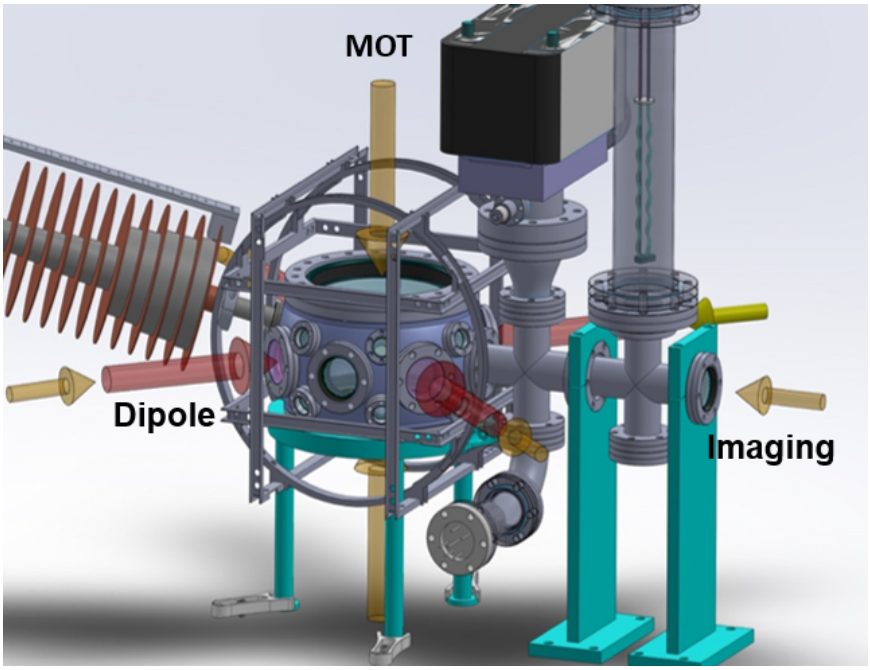

Figure 3.7: Schematic of MOT, dipole and imaging beams entering the main experimental chamber.

The MOT repumping beams are split into two pairs of counter-propagating beams with a projected dark spot in each beam's center. The crossing of the projected dark spot beams creates a spherical dark spot in the center of the MOT. The dark spot enhances the density of cold F = 1 atoms in the center of the MOT. On the experiment table, we use large 2" polarizing beamsplitter cubes and large 1.5" $\frac{\lambda}{2}$ - wave plates to control the polarization and power of each of the six MOT beams separately. Large 2" mirrors are used to direct the beams into the chamber with a configuration shown in Fig. 3.7. The MOT beams have a diameter of $\sim$ 1.25" to ensure a large

trapping volume. Photos of the experiment table, atomic beam fluorescence, and MOT fluorescence are shown in Fig. 3.8.

3.3.2 AOM and Shutters

In our experiment, we require remote control over the power and frequency of the laser beams to lower the temperature of the ultracold atomic cloud to reach sub-Doppler temperatures. We use acousto-optic modulators (AOM) as shown in Fig. 3.5 and Fig. 3.6 to change the intensity and the detuning of each of the laser beams. The switching times of the AOMs are on the order of ns so they can also be used to switch off the beams. However, to avoid the residual leakage light, we use mechanical shutters in addition to AOMs to turn off the light completely. The shutters turn off in a few ms and have to be carefully timed. We use a variety of AOMs from ISOMET and Gooch & Housego at frequencies between 40 MHz and 250 MHZ to achieve the necessary detunings. AOM drivers were purchased from Isomet, Gooch & Housego and Intra-action. To generate the repumping beams with larger detunings of $\sim$ 1.8 GHz, we use a fast AOM with a center frequency of 1.8 GHz and a bandwidth of 200 MHz by Brimrose (Brimrose GPF-1800-200-589) with a custom driver based on an Agilent synthesizer and Mini-Circuits 4 W RF-amplifier. In the next chapter, I will describe the imaging system that I built.

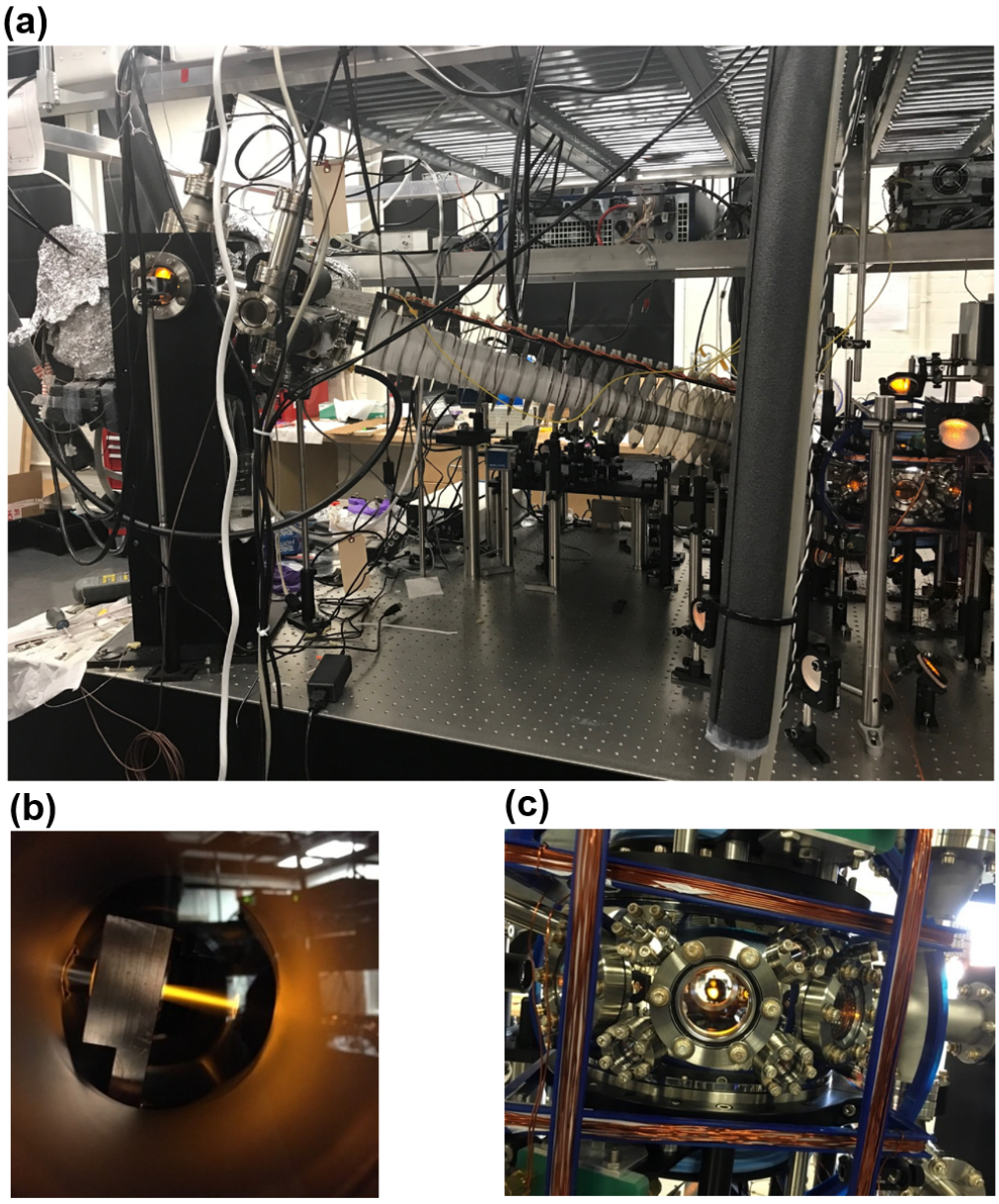

Figure 3.8: (a) Photo of the vacuum system built in our lab. (b) Fluorescence observed in oven. (c) Main experimental chamber photo with bias coils and MOT fluorescence inside the chamber.

Chapter 4

Imaging System

4.1 Introduction

Ultracold atomic clouds trapped in a vacuum chamber are small, typically around 5 μm to 8 mm in diameter, and spatial imaging techniques are easy methods to interrogate the atomic cloud and extract quantitative information like shape, size, atomic number density and temperature. I have implemented imaging via two common techniques: fluorescence and absorption imaging. These techniques are used to determine the physical properties of the atomic cloud. For quantitative measurement we prefer absorption imaging over fluorescence imaging, since it does not require knowledge of the solid angle of collected light to determine the atom number. In our experiment, fluorescence imaging is used only to monitor the MOT qualitatively as the MOT can move and become distorted if there is an imbalance in the intensity of cooling beams [53]. As the MOT is small and dense, it is difficult to achieve a good quantitative fluorescence imaging because of motional blurring and optical thickness [54]. Therefore, in our experiment we use laser-illuminated absorption imaging to probe the ultracold atoms and obtain important properties such as optical density, number density and atom number in the cloud. In the following sections, I start with a brief discussion of the theory and then describe the experimental design of my imaging system.

4.2 Theory

4.2.1 Optical Resolution

The optical resolution of any imaging system quantifies the capability of the system to determine the details in an object being imaged. Every optical system has its own

optical resolution. In the ideal case of thin lenses and no aberations, resolution is determined using numerical aperture (NA) given in air by $\frac{r}{d}$ where r is the radius of the lens and d is focal length of the first lens. The fundamental limit of resolution is determined by the diffraction limit. When a smallest possible spot size is imaged through a lens, its image is not a spot but forms an Airy disc because of diffraction, as seen in Fig. 4.1. The radius R of the Airy disc is defined as the radial distance from the center maximum to the first minimum. Far from the aperture, it is given by

$$R = \frac{1.22\,\lambda}{NA},$$

where NA is the numerical aperture and λ is the wavelength. Diffraction increases when the size of the lens aperture decreases and vice versa. Therefore, resolution can be optimized by optimizing the lens configuration. However, the resolution of a real imaging system is also limited by imperfection and misalignment in the lens configuration and the aberations due to non-ideal lenses.

4.2.2 Absorption Imaging

Absorption imaging is a standard method to probe the atomic cloud in situ and in time-of-flight [2] and is the method of choice used in our experimental setup. This technique measures the total excitation by an absorber and thus can be viewed as the most efficient technique for imaging [55]. In absorption imaging, a probe beam of resonant light is illuminating the atomic cloud and the shadow of the cloud is imaged onto a CCD camera using a lens configuration. The absorption of the resonant light forms a shadow on the CCD camera. Absorption imaging for atomic clouds works best in the regime where the cloud is thin with the optical density equal to or lower than one, and when the intensity of the probe beam is very weak, e.g. much lower than the saturation intensity. Otherwise, nonlinear effects such as saturation play a non-negligible role and complicate the analysis [56].

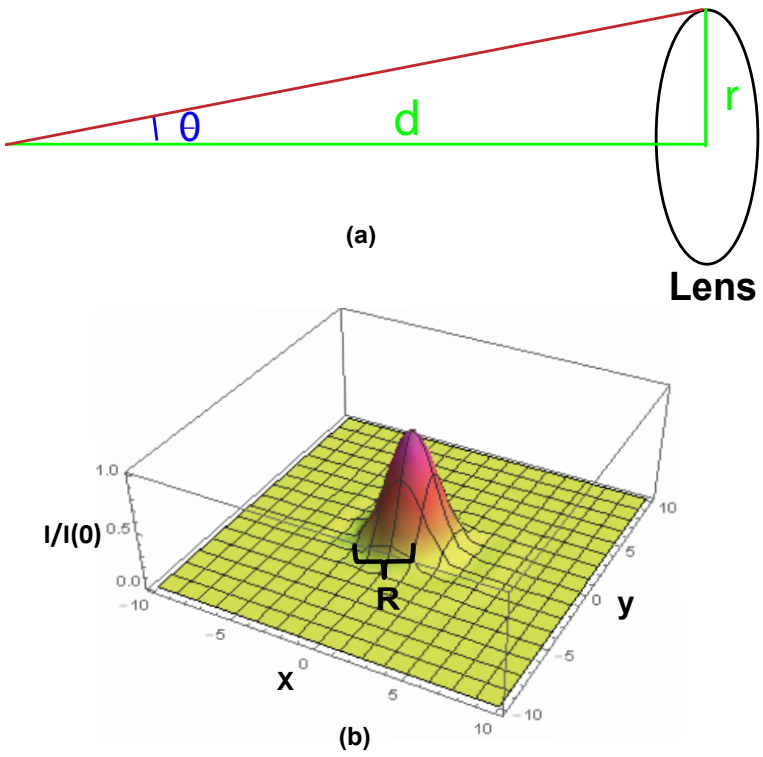

Figure 4.1: Physical parameters of the lens that affect the diffraction limit. (a) Schematic of lens configuration to observe diffraction, where θ is the maximum half-angle of the cone of light that enters or exits the lens, r is the radius of the lens, and d is the focal length. (b) Plot of the resulting Airy disc Bessel function profile. Here R is the radius of the Airy disc, x and y are spatial coordinates in arbitrary units, and $\frac{I}{I(0)}$ is the relative intensity in the image plane.

The intensity profile of a low intensity probe beam after the absorption follows the Lambert-Beer Law

$$I(y,z) = I_0(y,z)\exp^{-OD(y,z)} \tag{4.1}$$

where $I_0(y,z)$ is the initial intensity profile of the probe beam and OD(y,z) is the optical density profile. It is given by

$$OD(y,z) = \sigma\, n(y,z) = \sigma \int_{-\infty}^{\infty} n(x,y,z)dx \tag{4.2}$$

where n is the number density, x is the propagation direction of the imaging beam

and σ is the absorption cross section. σ depends upon the intensity, polarization and detuning of the probe beam as

$$\sigma = \frac{\sigma_0}{1 + 4(\frac{\Delta}{\Gamma})^2 + (\frac{I}{I_{sat}})} \tag{4.3}$$

where σ_0 is the on-resonance cross section which depends on the light polarization and atomic transition, Δ is the detuning of the imaging light from the atomic resonance, Γ is the natural linewidth of the optical transition, I is the intensity of the imaging light and I_{sat} is the saturation intensity. Normally, we try to be far below the saturation intensity which means that we can neglect the $\frac{I}{I_{sat}}$ term. To calculate the optical density from CCD images, three images are taken. Using those three images the relative intensities are computed to obtain the optical density profile as

$$OD = -\ln \frac{I(y,z)}{I_0(y,z)} = \ln \frac{I_{ref} - I_{bg}}{I_{raw} - I_{bg}} \tag{4.4}$$

Here, I_{raw} is the first image which includes both the cloud and the laser beam, I_{ref} is a second image taken without the atom cloud, but with the same imaging pulse with the same exposure as used for I_{raw}, and I_{bg} is a last image taken of the background with the laser switched off. This method has a disadvantage when the resonant probe beam falls on an atomic cloud that forms a BEC: it heats up the cloud and destroys the coherent condensate instantaneously. Therefore, when imaging BECs, a new condensate has to be prepared for every image to do the measurement correctly [57].

4.3 Design Of The Imaging System

4.3.1 Simulation and Calibration

The schematic outline of the optical setup, used for both fluorescence and absorption imaging, is shown in Fig. 4.2. The design is simulated using the software package OSLO to find the best lens configuration and optimum focal length to give high

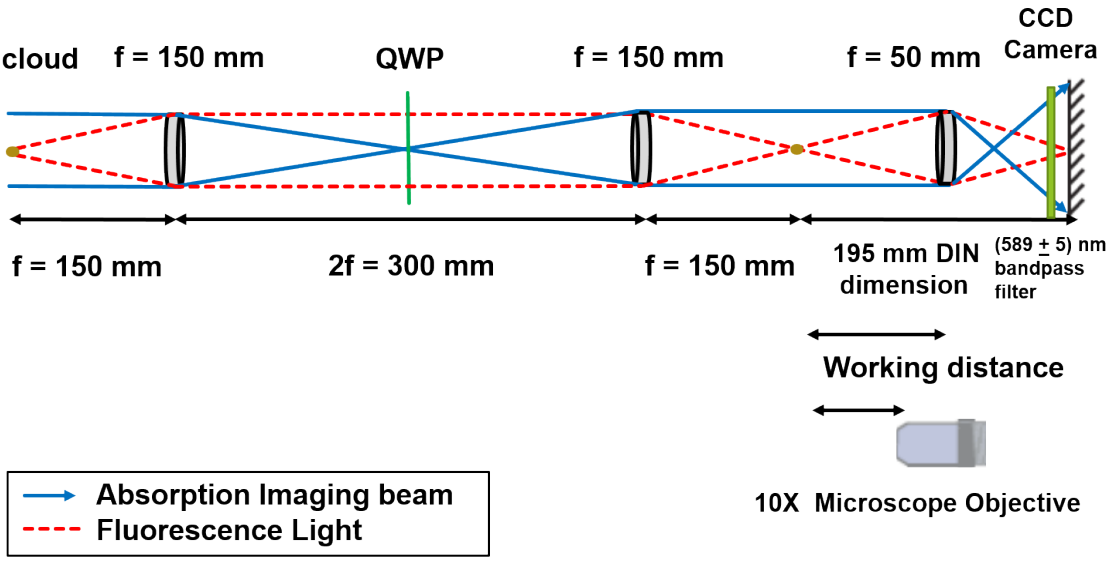

Figure 4.2: Schematic diagram of the optical configuration used for our imaging system. The lenses are achromatic doublets (47718 and 47713 for side imaging and 49285 and 49284 for top imaging) from Edmund Optics and the microscope objective (10 × DIN achromatic finite objective) is also from Edmond Optics. QWP is an abbreviation for quarter wave plate.

resolution $\sim \mu$m and variable magnification from m = 0.6 for imaging the MOT to m = 10 for imaging the BEC. This is necessary because of the orders of magnitude difference between the size of the MOT cloud ($\sim$ 8 mm) and BEC ($\sim$ 5 μm) to insure that each will fill out a large area of the CCD screen. With the help of OSLO, I find that achromatic doublet lenses in a relay telescope configuration best fit our spatial constraints around the chamber, with the optimum focal length of f = 150 mm to give the minimum area point spread function and thus the highest resolution. The variable magnification of m = 0.6 and m = 10 is achieved by placing either a third lens with f = 50 mm, or a microscope objective with m = 10 (NA = 0.25), respectively.

A National Bureau of Standards resolution target (R2L2S1P1 NBS 1963A with

resolution up to 228 lines per mm) is used to measure the resolution and test the numerically predicted resolution and magnification values. The calibration test is conducted on the optical table by imaging the target in place of the atomic cloud using 589 nm laser light. The sharpness of the edges of the lines acquired using the target helps to determine the realistic resolution whereas the background noise and fringes in the test images give an idea on the sensitivity of the imaging system. The finest lines that we can resolve using our lens system with m = 0.6 is 45 lines per mm, corresponding to 11.1 μm resolution. When the microscope objective (Edmund Optics, 10 $\times$ DIN achromatic finite objective) is used to give m = 10, 128 lines per mm can be resolved and this corresponds to 3.9 μm resolution. Magnifications are measured using the ratio of object size to image size. The image size is determined by calculating the distance on screen when the image is in focus using the number of pixels. The object size is calculated using the known number of lines per cycle on the target. The magnification values measured this way are m = 0.56 for the lens and m = 8.8 for the microscope objective, these values are close to the theoretical values. Since the pixel size of the camera is 6.45 μm x 6.45 μm, this design ensures that we will be able to image both the MOT and the BEC atoms with many pixels without cropping. Although the smallest structure we will image is a BEC with a radius of around 5 μm, the imaging system we are using will magnify the atomic cloud by 10X so that it covers several pixels. The resolution of the imaging system then will correspond to 6 pixels and the size of the cloud to $\sim$ 15 pixels, allowing us to image the shape of the cloud.

4.3.2 Implementation of the Imaging System

Absorption imaging is used for the detection of the ultracold atomic cloud from the top and side of the vacuum chamber. The actual setup used for imaging is shown

in Fig. 4.3. The relay telescope is used to minimize the working distance for the microscope objective so that the objective can be placed before the CCD camera and all optics can be outside of the vacuum chamber.

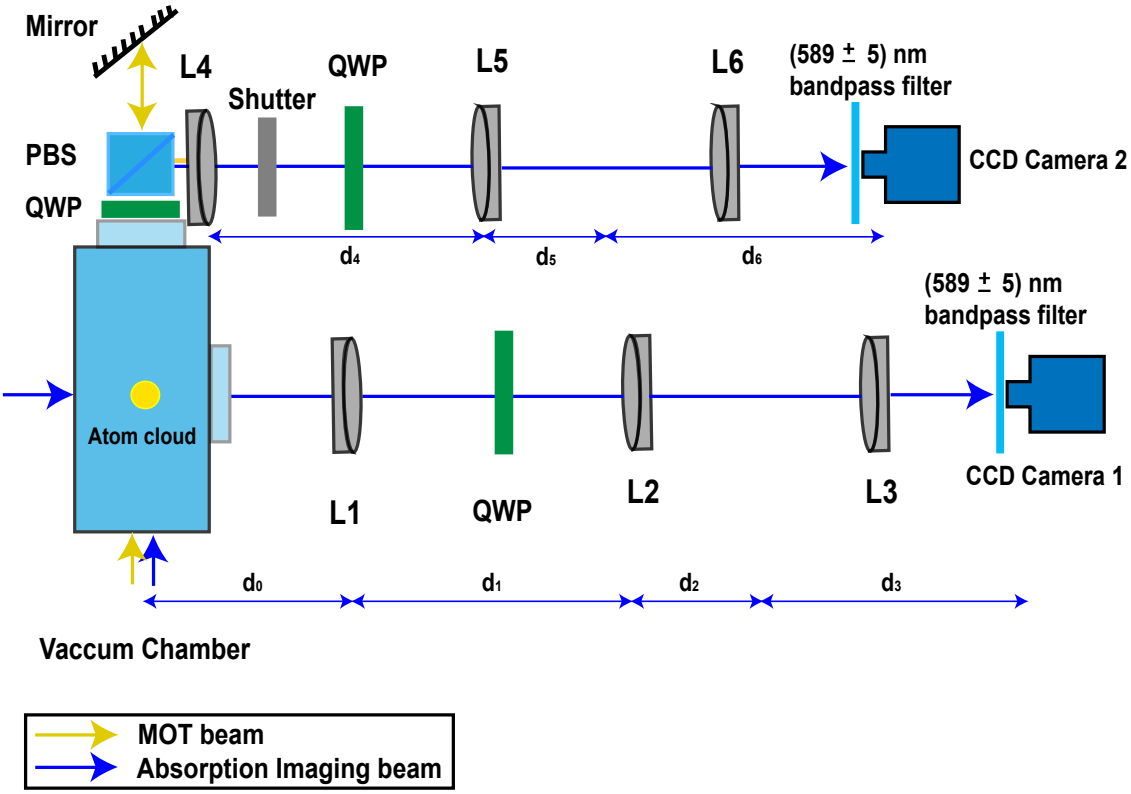

Figure 4.3: Top and side imaging system used to take absorption images of the ultracold atomic cloud formed inside our vacuum chamber. CCD Camera 1 along with the lenses L1, L2 and L3 with quarter a wave plate (QWP) in the center of L1 and L2 make up the side imaging system. CCD Camera 2 along with the lenses L3, L4 and L5 with a quarter wave plate (QWP) and mirror placed on the top window of the vacuum chamber forms the top imaging system. The diagram is not to scale. The distances are $d_0 = 150$ mm, $d_1 = 300$ mm, $d_2 = 150$ mm, $d_3 \approx 195$ mm, $d_4 = 300$ mm, $d_5 = 150$ mm, $d_6 \approx 195$ mm. The distance from the cloud to the first lens for top imaging is also 150 mm.

The system consists of two identical achromatic doublet lenses with f = 150 mm for both top (Edmund Optics, 49285 lens ach 50 × 150 vis 0 ts) and side (Edmund Optics, 47718 lens ach 30 × 150 vis 0 ts) imaging and one achromatic doublet lens with f = 50 mm (Edmund Optics, 47713 lens ach 30 × 50 vis 0 ts) for side and f = 100 mm (Edmund Optics, 49284 lens ach 50 × 100 vis 0 ts) for top imaging. The purchased microscope objectives (Edmund Optics) used have magnification of m = 4 (NA = 0.1) and m = 10 (NA = 0.25). They are AR coated and designed for visible light (400 nm-700 nm).

I found that the Thorlabs cage system for 1" optics is not stable enough and therefore was not used for our system. A Thorlabs alignment target helps to align the beam for our imaging system.

To reduce interference fringes in the absorption imaging, we place a quarter-wave plate in the center of the telescope. The wave plate prevents etaloning between the two lenses as the light beams bouncing back and forth in the telescope are orthogonally linearly polarized to each other [58]. It minimizes most of the fringes and allows us to achieve better image quality. An index card is used to see the shadow of the atomic cloud close to the CCD screen while both MOT and imaging beam are switched on continuously which helps to center the cloud in the vacuum chamber.

The cameras used are high performance CCD cameras from PCO (PCO Pixelfly USB) with 14 bit dynamic range. Table 4.1 provides the most important specifications of our cameras. The cameras are placed on a precise translation stage with micrometer screws to adjust the focus. The stage allows us to move the camera in the x and y direction. The camera can also be moved in the z direction by adjusting a Thorlabs post holder.

Table 4.1: Camera Specification

Quantity	Specification
Type of sensor	CCD
Quantum efficiency	62 %
Dynamic range A/D	14 bit
Pixel size	6.45 μm $\times$ 6.45 μm
Resolution	1392 $\times$ 1040 pixel
Size	39 mm $\times$ 39 mm $\times$ 71 mm
Double Shutter Mode	2 images in rapid succession $\sim\mu$s

4.3.3 Fringe Reduction for Absorption Images

We take images to study the physical properties of the ultracold atoms by measuring the atom number and size of the cloud. Therefore, to accurately measure the atom number it becomes important to remove all the fringe patterns and inhomogeneities and use high quality imaging beam profiles, ideally perfectly Gaussian beams. In practice, the imaging beam always contains multiple overlapping fringe patterns due to passing multiples lenses, windows and wave plates with dust on them. In addition etaloning of the imaging beam between optics creates interference fringes that are very sensitive to vibration. We place a quarter wave plate in the center of the telescope to reduce some interference fringes from the absorption images. But there are other sources of noise in the imaging process. For example, I found that the fringes shown in Fig. 4.4(a) are caused mostly by residual mechanical vibration of the camera.

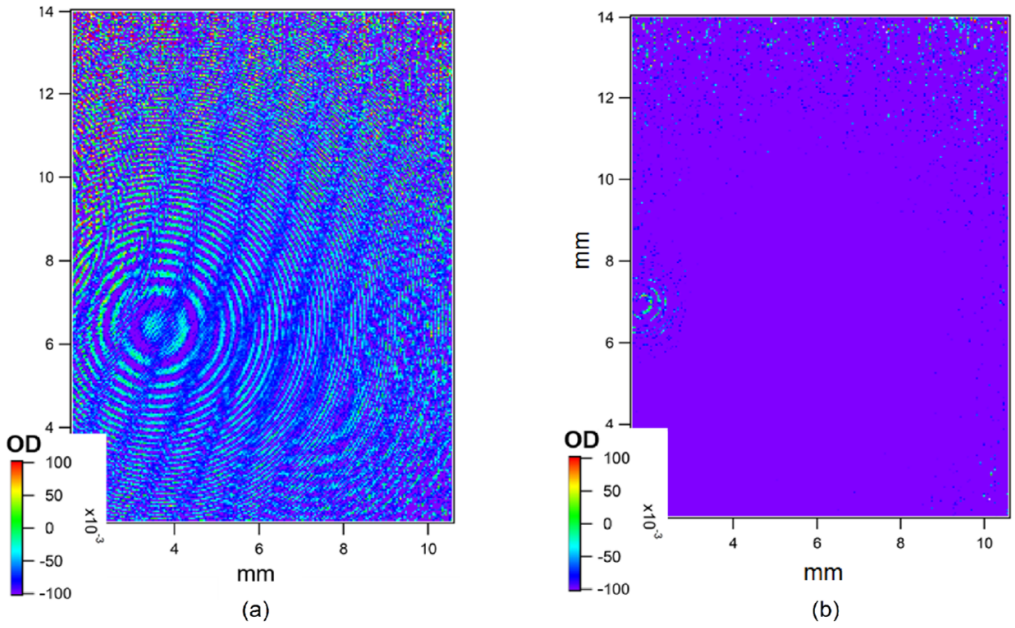

Figure 4.4: (a) Absorption image with fringes produced due to camera vibration. (b) Absorption image without fringes after minimizing the camera vibration.

If there is a large time elapsed between the background image and the image with atoms then a mismatch occurs which produces patterns shown in Fig. 4.4(a). The mechanical vibration of the lenses and camera can change the intensity profile of the imaging beam between the two images and create those fringes on absorption images. Therefore, to reduce the mechanical vibration we simply firmly secure all the optics in our imaging setup. I am using a 0.5 inches wide and 8" long Thorlab posts for all the lenses and wave plate. I found that it is important to firmly mount the camera on a thick 1" post to prevent any small vibrations that caused spurious fringes in the images after subtraction. After reducing all the mechanical vibrations I obtained better quality images as shown in Fig. 4.4(b).

4.3.4 Data Acquisition

Our imaging system is controlled from two main desktop computers via LabVIEW. The first computer is used to run the experiment sequence via 2 NI DAQ analog output boards and 1 Spincore Pulseblaster digital output board. The sequence is shown in Fig. 4.5 for the molasses. The remote computer control and the optimization of the laser cooling sequence are the topic of the next chapter. The second computer is used to run the camera software and store the images taken after each experiment is performed. The images stored are analyzed automatically using IGOR software.

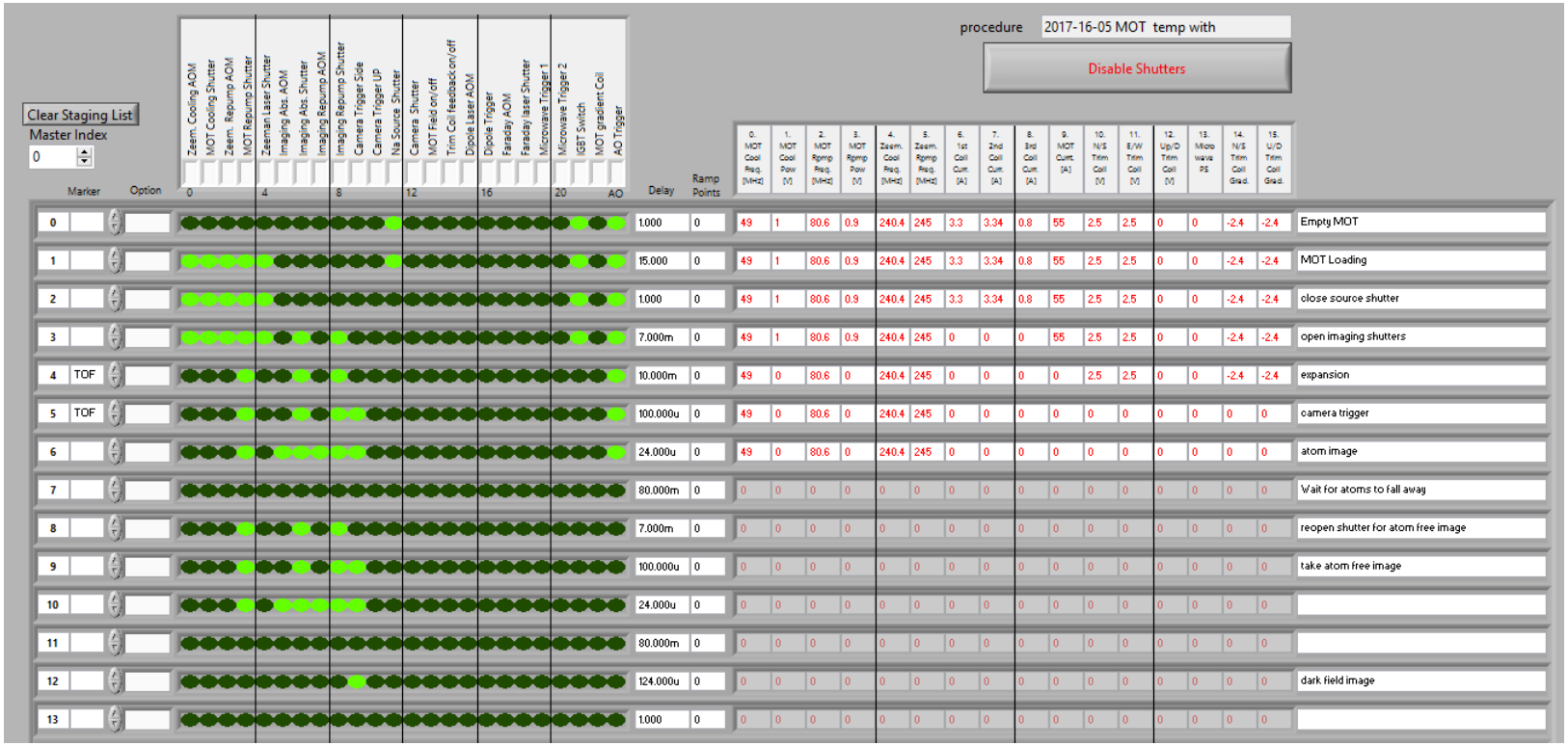

Figure 4.5: Screen shot of the LabVIEW program used to control our experiment via timing of 16 analog and 24 digital output voltage channels.

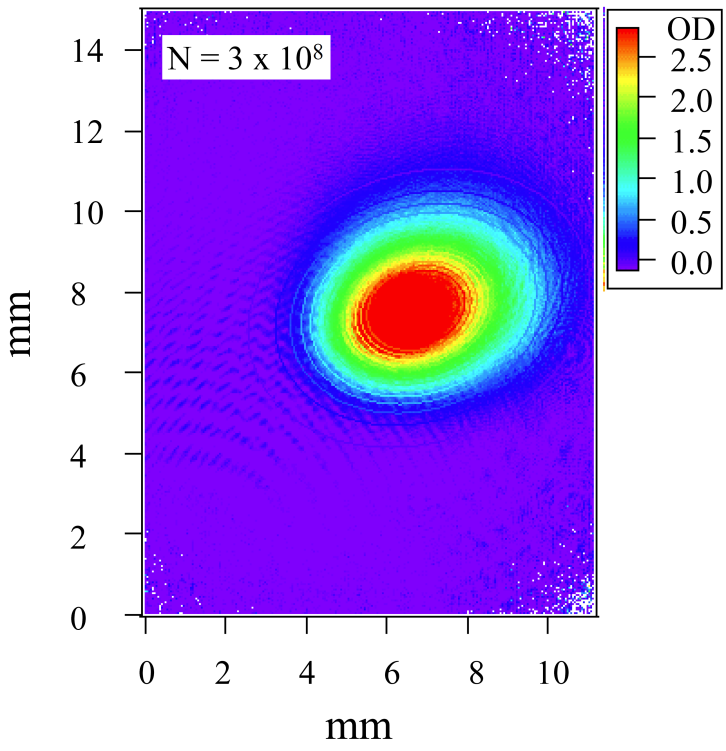

Figure 4.6: Typical false-color absorption image of the MOT after a short optical molasses phase. The atom number is determined by a 2D Gaussian fit to the absorption profile. The fit is done automatically for each repeat of the timing sequence in the IGOR PRO analysis software.

The CCD camera is trigged using LabVIEW on the main computer and three consecutive images are received by the second computer as referred in 4.2.2. Each time a sequence of three images is received, they are automatically converted to optical densities and a Gaussian 2D fit is made for each OD profile to calculate the various physical quantities of the atomic cloud such as atom number, size and density. An example of an absorption image of the atomic cloud with number measurement and optical density is shown in Fig. 4.6. We use two computers because the analysis with 2D Gaussian fits can sometime cause a large CPU load and slow down the analysis computer. However, this slowing down will not disturb the experiment sequence that

is running on the other computer. Thousands of images were analyzed to optimize the cooling sequence, as detailed in the next chapter.

Chapter 5

Optimized Laser Cooling of Na atoms

5.1 Introduction

The atom number and temperature of the cloud are the two most important parameters that need to be optimized to successively load the atomic cloud to an optical dipole trap [59] and cool down the atoms further by evaporative cooling to get to the BEC regime. In this chapter I describe how these two physical properties of the atom cloud were optimized.

5.2 Optimization Goals

After observing the MOT, the next important process is to maximize the number of the atoms in the MOT by optimizing the laser (MOT Cooling, MOT Repump, Zeeman Cooling, Zeeman Repump) frequencies, Zeeman slower currents in all three segments as discussed in section 3.2.3 and bias coil current in all three direction (x, y, z) discussed in section 3.2.4 (ii). After achieving the maximum atom number, the second most important objective is to lower the temperature of the cold cloud below the Doppler limit to make it cold enough to load efficiently into the optical dipole trap (trap depth $\sim$ 1 mK) [1]. This is done by implementing polarization gradient cooling (PGC) in an optical molasses phase. Each of these phases consists of several sub-phases where laser parameters (power and frequency) and magnetic fields are changed. These phases and sub-phases are discussed in detail in the following sections.

5.3 Theory

5.3.1 Optical molasses

Typically, before loading the atoms from the MOT into an optical dipole trap in which they can be further cooled, the atoms are subjected to a short phase of optical molasses with a duration of 1 to 100 ms to further lower the temperature of the cloud [59, 60]. Until 1985, the Doppler limit which is $\sim 240\ \mu$K for Na^{23}, was thought to be the theoretical lowest value of the temperature of atoms that could be obtained by laser cooling, but a group at Bell Laboratories proved this estimation wrong by obtaining temperatures much lower than the Doppler limit with the first observation of optical molasses [8]. Optical molasses is one of the laser cooling techniques that cools atoms in a region in a vacuum chamber by intersecting three pairs of counterpropagating laser beams inside the chamber. MOT and optical molasses are similar to each other except that there is a magnetic field present in the MOT to compress and trap the atomic cloud. The spatially dependent restoring force formed by the magnetic field in the MOT is eliminated in the molasses phase by quickly switching off all the magnetic fields. Optical molasses is a cooling scheme, not a trap. The atoms' velocities are damped in an observational region by the laser light for a few tens of ms before atoms move out of the beam region. The damping of the velocities of the atoms is directly related to a reduction in temperature of the atoms as their kinetic energy is reduced. Surprisingly, in an optical molasses the temperature of the atoms is typically reduced by an order of magnitude compared to that of the MOT. The reason for this is polarization gradient cooling (PGC).

5.3.2 Polarization Gradient Cooling

The techniques that decrease the temperature of the gas below the Doppler limit are known as sub-Doppler cooling techniques. PGC is one of the most effective, simple

and fast sub-Doppler technique used in optical molasses [8]. In 1989, the groups of C. Cohen-Tannoudji [27] and S. Chu [61] proposed this mechanism of cooling and afterwards, researchers found that this method can be expanded to many areas of research among which gray optical molasses [62] was one of them. According to the PGC theory, the equilibrium temperature of the cold atomic cloud is given by [63]

$$T_e \approx \frac{C\,\hbar\,\Omega^2}{k_B \mid \delta \mid} \tag{5.1}$$

where C is a numerical factor on the order of 0.1, $\hbar$ is Planck's constant, Ω is the Rabi frequency, k_B is the Boltzmann constant and δ is the laser detuning. The equation shows that the temperature of the cold atomic cloud is inversely proportional to the detuning of the cooling laser for a given intensity and proportional to the intensity of the cooling laser for a given frequency. Therefore, detuning the laser more and lowering the power of the laser in PGC should decrease the temperature of the cloud, exceeding the Doppler limit. The ultimate limit of PGC is the recoil limit, the temperature associated with a single photon emission. For Na, the recoil limit is ~ 2 μK, two orders of magnitude lower than the Doppler limit.

5.3.3 Time of Flight

From the above discussions we conclude that the temperature measurement is one of the most important measurement for a cold atomic cloud if one is interested in eventually reaching the BEC regime. Several techniques have been derived to measure the temperature of a cold gas. Among all techniques, release and recapture (R&R) [8] and time of flight expansion (TOF) [64, 26, 65, 66] are the two which are most commonly used in cold atomic gas experiments. For our experiment we have used the TOF technique to obtain the temperature of both the MOT and the optical molasses as it is simple to implement compared to the to R&R method. TOF expansion lends itself well to atomic clouds that are too dense and small to be accurately imaged

optically. In our experiment TOF measurements are done by turning off the cooling beams and magnetic fields and imaging the falling cold atomic cloud using absorption imaging from the side with a weak probe beam. This method measures the momentum distribution of atoms, assuming the cloud expands ballistically. This momentum distribution is then used to calculate the temperature of the cloud via [67]

$$\omega(\tau) = \sqrt{\omega(0)^2 + \frac{T\,k_B}{M}\tau^2} \tag{5.2}$$

where $\omega(\tau)$ is the measured $\frac{1}{\sqrt{e}}$ half−width after expansion time τ, $\omega(0)$ is the initial width, T is the temperature, k_B is the Boltzmann constant and M is the atomic mass.

5.4 Computer Control

5.4.1 Hardware Timing

Experiments related to Bose-Einstein condensates require complicated timing sequences during which laser beam amplitudes and frequencies are changed, magnetic fields are ramped, shutters are switched, cameras are triggerd, and more. Most experimental parameters are therefore fully controlled by a computer system. In our experiment two computers are used to run the experiment and to analyze the data. Fully automated control and analysis of the laser cooling sequence is accomplished via 3 PCI DAQ boards that output digital and analog signals.

All three PCI boards are connected to the main computer. The analog signals are generated by two NI boards (PCI-6733) with eight analog output channels whereas the digital signals are generated by a SpinCore board (PB24-100-4K PulseBlaster) with 24 digital output channels clocked at 100 MHz. With the help of BNC cables these PCI boards send analog and digital signals to all our devices such as AOM mechanical drivers, mechanical shutters, power supplies and the CCD-cameras so that they are all controlled by the main computer. The three DAQ boards are controlled by a computer

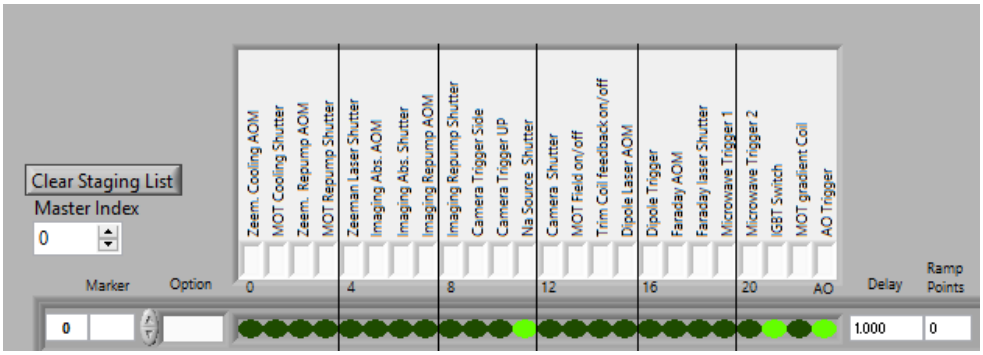

(a)

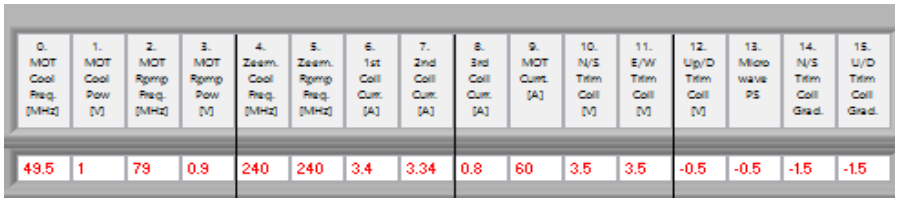

(b)

Figure 5.1: (a) The 23 digital channels: 22 digital channels are used to send digital pulses to all devices used in laser cooling experiment and the 23^{rd} channel is used to clock two PCI boards with analog channels to generate ramps and synchronize digital and analog signals. (b) The 16 analog channels (8 on each PCI board) used to generate analog voltages to send to the devices. The images are from the sequence created using LabVIEW used to perform our laser cooling experiment. Shown is one time slice of the sequence. Hundreds of slices can be stacked with arbitrary durations per slice between 10 ns and 60 s.

system using a sequencing program written in LabVIEW. The DAQ boards are kept outside the computer in a separate PCI Express to 4-slot PCI breakout box (Startech PEX2PCI4) with a long digital extension wire to situate all PCI cards close to the optical table and all outputs close to the devices that are controlled by them. This helps to minimize the length of the BNC cables which minimizes the analog signal cable length to reduce noise pickup.

5.4.2 Software

As mentioned above there are two computers used for the experiment. The main computer controls the hardware timing using LabVIEW. The secondary computer controls the camera settings and receives camera images using LabVIEW, and performs image analysis and plotting with IGOR. Using LabVIEW, exposure time, type of imaging (absorption or fluorescence), rate and delay time of the camera can be changed whereas using IGOR the region of interest, binning and fitting of the image of the atomic cloud can be adjusted, among other parameters. On the main computer, timing sequences are created with LabVIEW which helps to define and run each experimental procedure. The sequence is used to switch the laser beams via AOMs to change powers and the frequencies of the various beams, change currents of MOT coils, bias coils and Zeeman slower segments, open and close the mechanical shutters and trigger acquisition on the CCD camera by sending analog and digital voltages to those devices. The program can repeat a timing sequence automatically and can scan any parameters mentioned above. During each run, the three images of the cold cloud mentioned in section 4.2.2 are stored and displayed on the secondary computer. Physical properties of the cloud like number, density and temperature are automatically extracted using 2D Gaussian fits.

5.5 Cooling Sequence Optimization

5.5.1 Optimization Parameters

The goal of my optimization efforts was to achieve high atom number $\sim$ 600 million for the cold atomic cloud and sub-Doppler temperatures, T $<$ 240 μK. To achieve this goal various parameters were optimized. First the beam diameter of cooling and repump MOT beams was manually increased to around 2.5 cm to cool a larger volume.

Then all the AOMs shown in Fig. 3.3 were calibrated for frequency and amplitude and clamped within the input voltage limit of 0 to 1 volt as working at higher voltage may destroy the AOM drivers. Oven temperatures were also manually increased, actively servo-controlled and monitored so that the pressures in the oven and vacuum chambers remained around 10^{-8} Torr and 10^{-10} Torr respectively. The final temperatures of the oven under those pressure values which gave a strong MOT and high atom numbers are 345 °C for the reservoir and 415 °C for both back and front nozzle heaters. Finally, all the other parameters controlled by the timing sequence, e.g. bias coil currents, MOT coil currents, laser powers and frequencies, and the Zeeman slower segment currents were optimized by automatically scanning each parameter using sequences created on the main computer.

5.5.2 Zeeman Slower Optimization

Our Zeeman slower solenoid segments are designed to compensate the Doppler shift and allow slowing of atoms that exit the oven nozzle with longitudinal velocity components of $v \leq 700\ \frac{m}{s}$ to $v \leq 20\ \frac{m}{s}$, which is the capture velocity of the MOT. The design currents for segments are 4 A but we found that a tweaking of the currents improved the atom number in the MOT. Therefore, optimization of all three segments was done by monitoring the atom number in the MOT. It is difficult to find the optimum current value for all three segments at a time. So, I automatically scanned two segment currents with stepsize of 0.05 A using the LabVIEW sequence and then plotted the resulting atom number in a contour plot as shown in Fig. 5.2 to find the optimized current values.

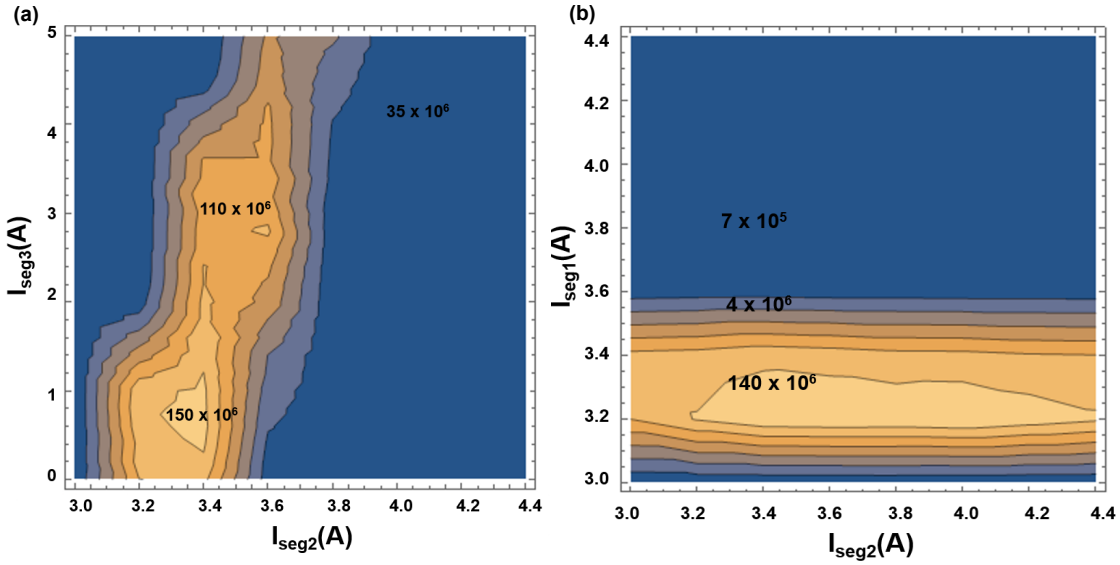

Figure 5.2: (a) The plot shows the MOT atom number as a function of Zeeman slower segment 2 and segment 3 current. The optimized values found are 3.34 A for segment 2 and 0.8 A for segment 3.(b) The plot shows the MOT atom number as a function of Zeeman slower segment 2 and segment 1 current. The optimum values found are 3.34 A for segment 2 and 3.3 A for segment 1.

We found a strong dependence of the trapped atom number on the current in segment 3 which is used to select the final velocity. This was expected since a large current in segment 3 can push atoms back into the slower tube intead of allowing atoms to reach the MOT capture volume. The Zeeman slowing beam and Zeeman repump beam detunings were also optimized. A strong dependence on the slowing beam was observed and the design value gave the best results. When changing the Zeeman slower repump detuning, only weak dependency was observed over a range of $\sim$ 30 MHz.

5.5.3 Optical Molasses Optimization

To ensure the pressure in the experimental chamber is low enough for future evaporative cooling in the dipole trap, which can take several seconds, the lifetime of the MOT was first measured. The $\frac{1}{e}$ lifetime, τ, of the MOT was determined by an exponential fit to the long time tail of the decay curve, resulting in $\tau = 23.5 \pm 5.4$ s as shown in Fig. 5.3. The temperature of the MOT is found to be 700 ± 14 μK with $(6.0 \pm 0.3) \times 10^8$

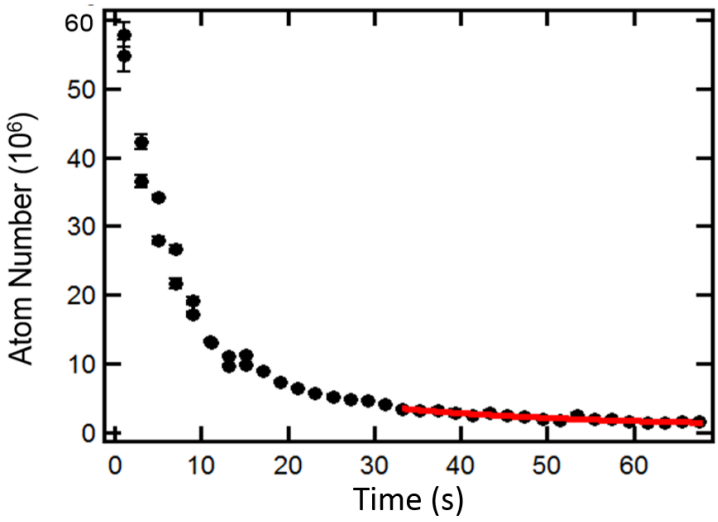

Figure 5.3: Plot of MOT decay time in experimental chamber. The line is an exponential decay fit for long times to determine the lifetime of the MOT to ensure low background pressure. The fit gives a lifetime of (23.5 ± 5.4) s.

atoms as shown in Fig. 5.4, before implementing PGC in optical molasses.

First, to optimize the optical molasses, a manual adjustment of cooling and repumping beam balance and bias coil current was done while lowering the quadrupole magnetic field to ensure a fluorescent cloud was observable at the lowest possible quadrupole field.

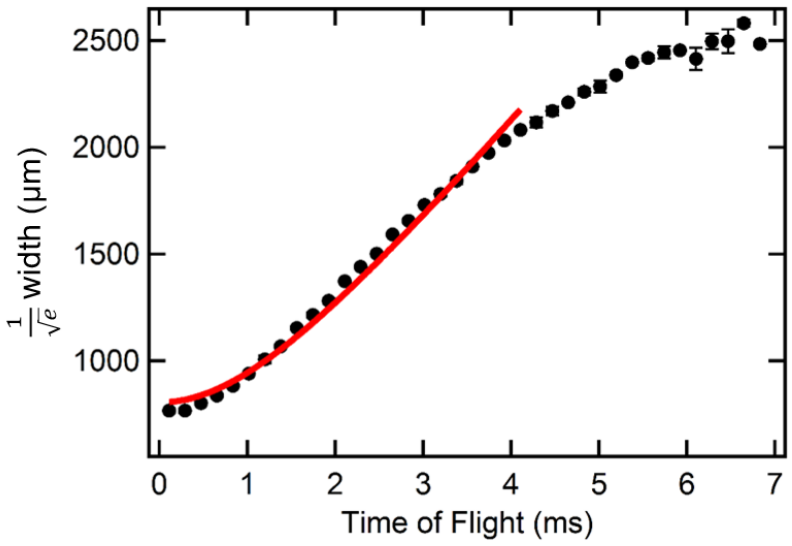

Figure 5.4: Time of flight expansion of $\frac{1}{\sqrt{e}}$ width of the MOT. The $\frac{1}{\sqrt{e}}$ width was obtained from Gaussian fits to absorption images. The line is a fit to Eq. 5.2. The fit gives a temperature of (700 ± 14)μK.

After doing these manual adjustments, the empirically found best PGC scheme, presented in Fig. 5.5, is programmed in the computer control experimental sequence to further lower the temperature. Table 5.1 shows the best parameters used for PGC which lowered the temperature from 700 ± 14 μK to 65.0 ± 0.1 μK as shown in Fig. 5.6 for an atomic cloud in a pure optical molasses with 2×10^8 atoms. This temperature should be low enough to load the crossed optical dipole trap (trap depth $\sim$ 850 μK) with a few million atoms and proceed to further lower the temperature of the cloud in the dipole trap via evaporation cooling to reach BEC.

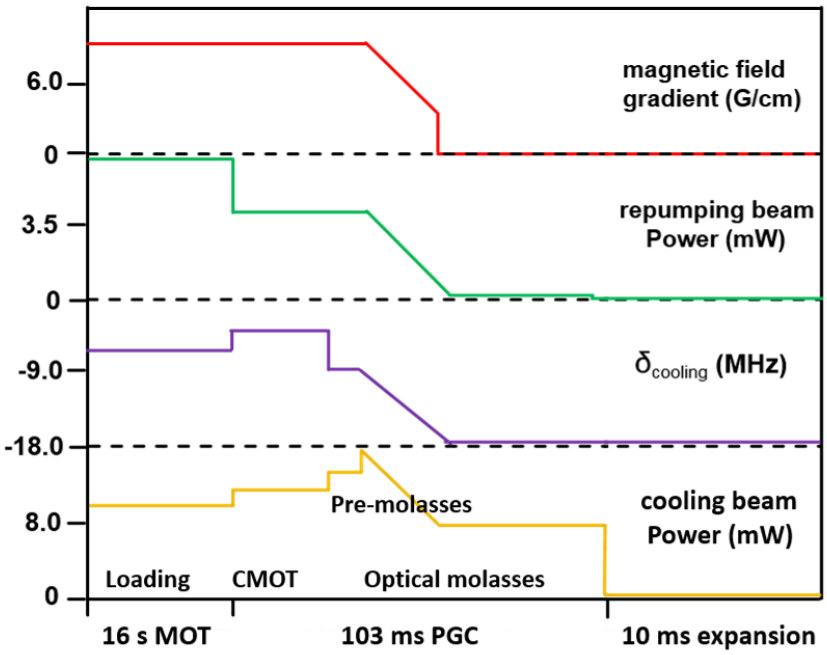

Figure 5.5: Empirically optimized experimental cooling sequence for optical molasses using polarization gradient cooling.

Table 5.1: Overview of molasses sequence

Process	Duration
Empty MOT	1s
Load MOT	16s
Source Shutter Off	500ms
Laser Shutters Open	7ms
Zeeman Slower Segments Off	1s
Optical Molasses	78ms
TOF (Free Expansion)	10ms

Table 5.2: Overview of bias coils current for both MOT and molasses phases

Bias Coils	MOT	molasses
X	2.5 A	0.50 A
Y	0.0 A	0.45 A
Z	-2.4 A	-1.15 A

The PGC stage lasts for 103 ms, where for the first 20 ms the MOT is compressed by increasing cooling power to 12 mW and decreasing repumping power to 3.5 mW. In this step the detuning of the MOT is also changed to -5 MHz. The MOT cooling beam power is then increased to 14 mW and further red detuned to -9 MHz for another 5 ms. Then, finally, 78 ms of optical molasses with 18 ms long ramp is applied to lower the temperature. In the optical molasses phase the MOT power is ramped to 8 mW from 16 mW and the repumping power is ramped to 0.3 mW. The MOT cooling detuning is ramped to - 17.5 MHz. The magnetic field gradient is also ramped down to 3.5 $\frac{G}{cm}$ from 10 $\frac{G}{cm}$ and finally to zero for the last 60 ms of the optical molasses phase. The bias coil current for all 3 pairs of coils were different for the MOT and molasses sequence. Table 5.2 provides those values.

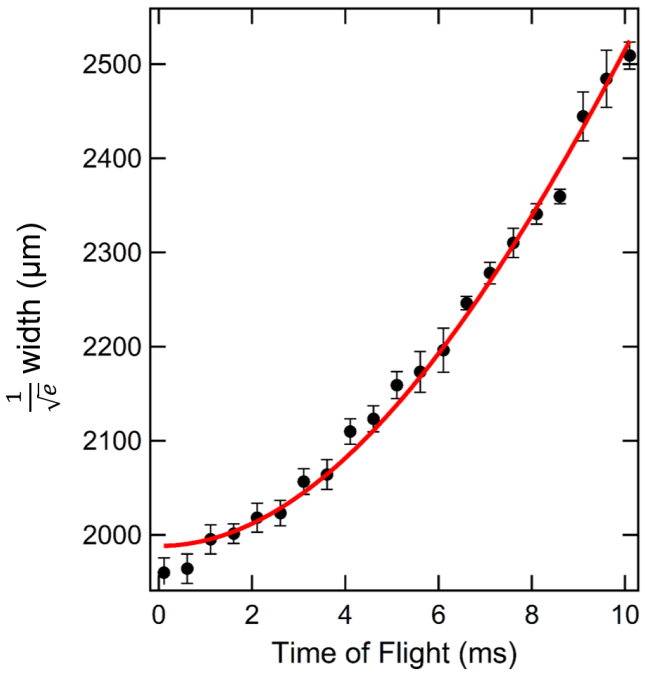

Figure 5.6: Time of flight expansion of $\frac{1}{\sqrt{e}}$ width of the optimized optical molasses. The $\frac{1}{\sqrt{e}}$ width was obtained from Gaussian fits to absorption images. The line is a fit to Eq. 5.2. The fit gives 65.0 ± 0.1 μK.

Chapter 6

Conclusion and Outlook

In conclusion, I implemented and tested an imaging system for an ultracold atomic sodium gas that allows for top and side imaging, absorption and fluorescence imaging and different magnifications. With the help of timing sequences and the automated absorption imaging, I optimized the number of trapped atoms in the MOT by optimizing parameters such as frequency, detuning, beam size of the lasers and stabilizing and adjusting the background magnetic gradient and fields. I then used the polarization gradient cooling technique successfully to lower the temperature below the Doppler temperature to $\sim (65.0 \pm 0.1)\ \mu K$ from an initially high temperature of the MOT of $\sim (700 \pm 14)\ \mu K$ while maintaining a large atom number of 200 million atoms in the trap.

The future plan is to implement evaporation cooling in a crossed far-off resonant dipole trap to further cool the atoms to quantum degeneracy and obtain BEC. After the realization of BEC, measurements on entanglement generation in spinor BECs will be performed to study matter-wave interferometry in spin space, and implement other devices using matter-wave quantum nonlinear optics in spin space, such as a phase sensitive amplifiers.

References

[1] D. A. Steck, "Sodium D line data," Los Alamos National Laboratory, Los Alamos **124**, (2000).

[2] W. Ketterle, D. S. Durfee, and S. D. M. Kurn, in *Making, probing and understanding Bose-Einstein condensates In Bose-Einstein Condensation in Atomic Gases*, edited by M. Inguscio, S. Stringari, and C. Wieman (IOS Press, (Proceedings of the International School of Physics "Enrico Fermi," Course CXL), 1999), Vol. 140.

[3] C. L. G. Alzar, P. G. Petrov, D. Oblak, J. H. Mueller, and E. S. Polzik, "Compensation of eddy-current-induced magnetic field transients in a MOT," arXiv preprint physics/0701251 (2007).

[4] M. H. Anderson, J. R. Ensher, M. R. Matthews, C. E. Wieman, and E. A. Cornell, "Observation of Bose-Einstein condensation in a dilute atomic vapor," Science **269**, 198 (1995).

[5] K. B. Davis, M. O. Mewes, M. R. Andrews, N. J. Van Druten, D. S. Durfee, D. M. Kurn, and W. Ketterle, "Bose-Einstein condensation in a gas of sodium atoms," Phys. Rev. Lett. **75**, 3969 (1995).

[6] A. Hansen, J. T. Schultz, and N. Bigelow, *Spin Textures and Topological Excitations in Spinor 87-Rb Bose-Einstein Condensates* (The Rochester Conferences on Coherence and Quantum Optics and the Quantum Information and Measurement meeting, OSA Technical Digest (online), Optical Society of America, 2013).

[7] J. M. Reeves, "An atom waveguide for interferometry with a Bose-Einstein condensate of rubidium-87," Ph.D. thesis, University of Virginia, 2006.

[8] S. Chu, L. Hollberg, J. E. Bjorkholm, A. Cable, and A. Ashkin, "Three-Dimensional Viscous Confinement and Cooling of Atoms by Resonance Radiation Pressure," Phys. Rev. Lett. **55**, 48 (1985).

[9] E. L. Raab, M. Prentiss, A. Cable, S. Chu, and D. E. Pritchard, "Trapping of neutral sodium atoms with radiation pressure," Phys. Rev. Lett. **59**, 2631 (1987).

[10] W. D. Phillips and H. Metcalf, "Laser deceleration of an atomic beam," Phys. Rev. Lett. **48**, 596 (1982).

[11] J. V. Prodan, W. D. Phillips, and H. Metcalf, "Laser production of a very slow monoenergetic atomic beam," Phys. Rev. Lett. **49**, 1149 (1982).

[12] H. J. Metcalf and P. Van der Straten, *Laser Cooling and Trapping* (Springer, New York, 1999).

[13] W. Ketterle, K. B. Davis, M. A. Joffe, A. Martin, and D. E. Pritchard, "High densities of cold atoms in a dark spontaneous-force optical trap," Phys. Rev. Lett. **70**, 2253 (1993).

[14] D. S. Naik, "Bose-Einstein condensation: Building the testbeds to study superfluidity," Ph.D. thesis, Georgia Institute of Technology, 2006.

[15] K. E. Gibble, S. Kasapi, and S. Chu, "Improved magneto-optic trapping in a vapor cell," Opt. Lett. **17**, 526 (1992).

[16] H. Wallis and W. Ertmer, "Fokker-Planck analysis of atomic beam cooling by frequency chirp methods," J. Phys. B **21**, 2999 (1988).

[17] M. Zhu, C. W. Oates, and J. L. Hall, "Continuous high-flux monovelocity atomic beam based on a broadband laser-cooling technique," Phys. Rev. Lett. **67**, 46 (1991).

[18] G. E. Marti, R. Olf, E. Vogt, A. Ottl, and D. M. Stamper-Kurn, "Two-element Zeeman slower for rubidium and lithium," Phys. Rev. A **81**, 043424 (2010).

[19] P. Cheiney, O. Carraz, D. Bartoszek-Bober, S. Faure, F. Vermersch, C. M. Fabre, G. L. Gattobigio, T. Lahaye, D. Guery-Odelin, and R. Mathevet, "A Zeeman slower design with permanent magnets in a Halbach configuration," Rev. Sci. Instrum. **82**, 063115 (2011).

[20] S. C. Bell, M. Junker, M. Jasperse, L. D. Turner, Y. J. Lin, I. B. Spielman, and R. E. Scholten, "A slow atom source using a collimated effusive oven and a single-layer variable pitch coil Zeeman slower," Rev. Sci. Instrum. **81**, 013105 (2010).

[21] C. J. Dedman, J. Nes, T. M. Hanna, R. G. Dall, K. G. H. Baldwin, and A. G. Truscott, "Optimum design and construction of a Zeeman slower for use with a magneto-optic trap," Rev. Sci. Instrum. **75**, 5136 (2004).

[22] F. Lison, P. Schuh, D. Haubrich, and D. Meschede, "High-brilliance Zeeman-slowed cesium atomic beam," Phys. Rev. A **61**, 013405 (1999).

[23] M. Barrett, J. Sauer, and M. Chapman, "All-optical formation of an atomic Bose-Einstein condensate," Phys. Rev. Lett. **87**, 010404 (2001).

[24] S. N. Bose, "Planck's Gesetz und Lichtquantenhypothese," Zeitschrift fur Physik **26**, 178 (1924).

[25] A. Einstein, "Quantum theory of the monoatomic ideal gas," Sitzungsber. Preuss. Akad. Wiss **1**, 3 (1925).

[26] P. D. Lett, R. N. Watts, C. I. Westbrook, W. D. Phillips, P. L. Gould, and H. J. Metcalf, "Observation of Atoms Laser Cooled below the Doppler Limit," Phys. Rev. Lett. **61**, 169 (1988).

[27] J. Dalibard and C. Cohen-Tannoudji, "Laser cooling below the Doppler limit by polarization gradients: simple theoretical models," J. Opt. Soc. Am. B **6**, 2023 (1989).

[28] C. C. Bradley, C. A. Sackett, J. J. Tollett, and R. G. Hulet, "Evidence of Bose-Einstein condensation in an atomic gas with attractive interactions," Phys. Rev. Lett. **75**, 1687 (1995).

[29] C. C. Bradley, C. A. Sackett, and R. G. Hulet, "Bose-Einstein condensation of lithium: Observation of limited condensate number," Phys. Rev. Lett. **78**, 985 (1997).

[30] S. L. Cornish, N. R. Claussen, J. L. Roberts, E. A. Cornell, and C. E. Wieman, "Stable 85 Rb Bose-Einstein condensates with widely tunable interactions," Phys. Rev. Lett. **85**, 1795 (2000).

[31] G. Modugno, G. Ferrari, G. Roati, R. J. Brecha, A. Simoni, and M. Inguscio, "Bose-Einstein condensation of potassium atoms by sympathetic cooling," Science **294**, 1320 (2001).

[32] T. Weber, J. Herbig, M. Mark, H. C. Nagerl, and R. Grimm, "Bose-Einstein condensation of cesium," Science **299**, 232 (2003).

[33] A. Griesmaier, J. Werner, S. Hensler, J. Stuhler, and T. Pfau, "Bose-Einstein condensation of chromium," Phys. Rev. Lett. **94**, 160401 (2005).

[34] S. Kraft, F. Vogt, O. Appel, F. Riehle, and U. Sterr, "Bose-Einstein Condensation of Alkaline Earth Atoms: Ca 40," Phys. Rev. Lett. **103**, 130401 (2009).

[35] S. Stellmer, M. K. Tey, B. Huang, R. Grimm, and F. Schreck, "Bose-Einstein condensation of strontium," Phys. Rev. Lett. **103**, 200401 (2009).

[36] M. Lu, N. Q. Burdick, S. H. Youn, and B. L. Lev, "Strongly dipolar Bose-Einstein condensate of dysprosium," Phys. Rev. Lett. **107**, 190401 (2011).

[37] K. Aikawa, A. Frisch, M. Mark, S. Baier, A. Rietzler, R. Grimm, and F. Ferlaino, "Bose-Einstein condensation of erbium," Phys. Rev. Lett. **108**, 210401 (2012).

[38] D. G. Fried, T. C. Killian, L. Willmann, D. Landhuis, S. C. Moss, D. Kleppner, and T. J. Greytak, "Bose-Einstein condensation of atomic hydrogen," Phys. Rev. Lett. **81**, 3811 (1998).

[39] D. M. Stamper-Kurn, M. R. Andrews, A. P. Chikkatur, S. Inouye, H. J. Miesner, J. Stenger, and W. Ketterle, "Optical confinement of a Bose-Einstein condensate," Phys. Rev. Lett. **80**, 2027 (1998).

[40] A. Widera, F. Gerbier, S. Folling, T. Gericke, O. Mandel, and I. Bloch, "Coherent collisional spin dynamics in optical lattices," Phys. Rev. Lett. **95**, 190405 (2005).

[41] Q. Gu, K. Bongs, and K. Sengstock, "Spin waves in ferromagnetically coupled spinor Bose gases," Phys. Rev. A **70**, 063609 (2004).

[42] C. D. Hamley, C. S. Gerving, T. M. Hoang, E. M. Bookjans, and M. S. Chapman, "Spin-Nematic Squeezing in a Quantum Gas," Nat. Phys. **8**, 305 (2012).

[43] D. Linnemann, H. Strobel, W. Muessel, J. Schulz, R. J. Lewis-Swan, K. V. Kheruntsyan, and M. K. Oberthaler, "Quantum-enhanced sensing based on time reversal of nonlinear dynamics," Phys. Rev. Lett. **117**, 013001 (2016).

[44] T.-L. Ho, "Spinor Bose condensates in optical traps," Phys. Rev. Lett. **81**, 742 (1998).

[45] D. M. Stamper-Kurn and W. Ketterle, in *Spinor Condensates and Light Scattering from Bose-Einstein Condensates*, edited by R. Kaise, C. Westbrook, and F. David (Springer, Berlin, Heidelberg, 2001), Vol. 72.

[46] J. Stenger, S. Inouye, D. M. Stamper-Kurn, H. J. Miesner, A. P. Chikkatur, and W. Ketterle, "Spin domains in ground-state Bose-Einstein condensates," Nature **396**, 345 (1998).

[47] J. P. Burke, C. H. Greene, and J. L. Bohn, "Multichannel Cold Collisions: Simple Dependences on Energy and Magnetic Field," Phys. Rev. Lett. **81**, 3355 (1998).

[48] N. N. Klausen, J. L. Bohn, H. Chris, and C. H. Greene, "Nature of spinor Bose-Einstein condensates in rubidium," Phys. Rev. A **64**, (2001), 053602.

[49] E. G. M. Van Kempen, S. J. J. M. F. Kokkelmans, D. J. Heinzen, and B. J. Verhaar, "Interisotope determination of ultracold rubidium interactions from three high-precision experiments," Phys. Rev. Lett. **88**, 093201 (2002).

[50] E. Mimoun, L. De Sarlo, D. Jacob, J. Dalibard, and F. Gerbier, "Fast production of ultracold sodium gases using light-induced desorption and optical trapping," Phys. Rev. A **81**, 023631 (2010).

[51] S. Q. Shang, Z. T. Lu, and S. J. Freedman, "Comparison of the cold-collision losses for laser-trapped sodium in different ground-state hyperfine sublevels," Phys. Rev. A **50**, R4449 (1994).

[52] K. Nasyrov, V. Biancalana, A. Burchianti, R. Calabrese, C. Marinelli, E. Mariotti, and L. Moi, "Magneto-optical trap operating on a magnetically induced level-mixing effect," Phys. Rev. A **64**, 023412 (2001).

[53] M.-S. Chang, "Coherent spin dynamics of a spin-1 Bose-Einstein condensate," Ph.D. thesis, Georgia Institute of Technology, 2006.

[54] M. Pappa, "Imaging Bose-Einstein condensates at ultra-low atom-numbers and time averaged adiabatic potentials," Ph.D. thesis, University of Crete, 2011.

[55] E. W. Streed, A. Jechow, B. G. Norton, and D. Kielpinski, "Absorption imaging of a single atom," Nat. Commun. **3**, 933 (2012).

[56] K. Hueck, N. Luick, L. Sobirey, J. Siegl, T. Lompe, H. Moritz, L. W. Clark, and C. Chin, "Calibrating high intensity absorption imaging of ultracold atoms," Opt. Express **25**, 8670 (2017).

[57] T. B. Ottenstein, "A New Objective for High Resolution Imaging of Bose-Einstein Condensates," Ph.D. thesis, Kirchhoff Institute of Physics, 2006.

[58] M. R. White, *Ultracold atoms in a disordered optical lattice* (University of Illinois at Urbana-Champaign, University of Illinois, Urbana-Champaign, 2009).

[59] R. Dumke, M. Johanning, E. Gomez, J. D. Weinstein, K. M. Jones, and P. D. Lett, "All-optical generation and photoassociative probing of sodium Bose-Einstein condensates," New J. Phys. **8**, 64 (2006).

[60] J. Jiang, L. Zhao, M. Webb, N. Jiang, H. Yang, and Y. Liu, "Simple and efficient all-optical production of spinor condensates," Phys. Rev. A **88**, 033620 (2013).

[61] P. J. Ungar, D. S. Weiss, E. Riis, and S. Chu, "Optical molasses and multilevel atoms: theory," J. Opt. Soc. Am. B **6**, 2058 (1989).

[62] G. Grynberg and J. Y. Courtois, "Proposal for a Magneto-Optical Lattice for Trapping Atoms in Nearly-Dark States.," Europhys. Lett. **27**, 41 (1994).

[63] J. Dalibard and C. Cohen-Tannoudji, "Laser cooling below the Doppler limit by polarization gradients: simple theoretical models," J. Opt. Soc. Am. B **6**, 2023 (1989).

[64] C. J. Cooper, G. Hillenbrand, J. Rink, C. G. Townsend, K. Zetie, and C. J. Foot, "The Temperature of Atoms in a Magneto-optical Trap," Europhys. Lett. **28**, 397 (1994).

[65] D. S. Weiss, E. Riis, Y. Shevy, P. J. Ungar, and S. Chu, "Optical molasses and multilevel atoms: experiment," J. Opt. Soc. Am. B **6**, 2072 (1989).

[66] T. M. Brzozowski, M. Maczynska, M. Zawada, J. Zachorowski, and W. Gawlik, "Time-of-flight measurement of the temperature of cold atoms for short trap-probe beam distances," J. Opt. B **4**, 62 (2002).

[67] J. Tallant, K. R. Overstreet, A. Schwettmann, and J. P. Shaffer, "Sub-Doppler magneto-optical trap temperatures measured using Rydberg tagging," Phys. Rev. A **74**, 023410 (2006).